Investigating superswells and sea level changes caused by superplumes via normal mode relaxation theory

V. R. Barletta[1] and R. Sabadini[1]

Received 1 July 2005; revised 14 December 2005; accepted 9 January 2006; published 8 April 2006.

[1] The superplume hypothesis, particularly for one in the mid-Cretaceous, has stimulated the search for evidence for or against such an event and the associated superswell. An approach based on normal mode relaxation theory makes it possible to simulate the surface deformation caused by the rising plume using a spherical, self-gravitating and stratified viscoelastic Earth model. The results for the superswell are consistent with those of previous analyses using convection and experimental modeling. The self-consistent coupling of elastic and viscous properties based on Maxwell rheology reveals that elasticity plays an important role contributing up to 30% to surface swelling when the plume head crosses the upper mantle. We show that the deformation at great distances from the superswell is relatively small, of the order of meters at most, and opposite in sign with respect to the large uplift over the plume, of the order of kilometers. The global subsidence over a wide region of the planet surrounding the superswell counteracts its effects on sea level changes and triggers a ''eustatic'' signal of a few meters at most, a negligible magnitude with respect to 250 m characteristic for the mid-Cretaceous. Previous arguments against the mid-Cretaceous superplume hypothesis, which assume that the large amount of water displaced by the superswell causes a ''eustatic'' sea level rise of about 200 m thus competing with the displacement due to oceanic crust production, are no longer tenable since such estimates did not account for the global behavior of the planet under internal loads.

Citation: Barletta, V. R., and R. Sabadini (2006), Investigating superswells and sea level changes caused by superplumes via normal mode relaxation theory, *J. Geophys. Res.*, *111*, B04404, doi:10.1029/2005JB003926.

1. Introduction

[2] There is no unanimous definition of plume, the term being used to indicate both buoyant rising material originating from the thermal boundary layer between the upper and lower mantle and extended regions of the lower mantle underlying surface superswells that are visible in seismic tomography. These latter regions are often referred to as ''mega-'' or ''super-plumes,'' and, although the terms can also indicate the ancient large plumes which originated from the boundary layer between the core and the lower mantle, superplumes have been put forward since the 1990s to explain large igneous provinces (LIPs) [*Larson*, 1991a, 1991b]. While the plume hypothesis is not universally accepted, it is hoped that refinements in seismic tomography capabilities will make it possible to arrive at an evidence for the existence of plumes [*Montelli et al.*, 2004]. *Morgan* [1971, 1972] suggests that plumes originate from the core-mantle interface and are due to local heating and rising of the buoyant material. Yet, since the 1990s other mechanisms have been proposed to explain the origin of the plumes [*Griffiths and Campbell*, 1990; *Dobrestov et al.*, 2003], and many superplume (and plume) features have been inferred from numerical fluid-dynamic models within Boussinesq approximation schemes [*Van Keken*, 1997; *Marquart et al.*, 2000] and laboratory experiments [*Griffiths and Campbell*, 1990]. Some of these features, i.e., shape, dimensions, excess temperature and the velocity of the rising material are the input data for our superplume simulation. These numerical and analogical models are generally flat, not spherical, Earth models. Furthermore, within the same scheme, they also estimated the lithospheric swell caused by the plume.

[3] The dynamic topography in this class of mantle fluid-dynamic models are usually worked out from an a posteriori evaluation of the normal stress at the surface of the fluid. However, the study of surface deformation induced by internal density anomalies can be performed via a totally different approach with respect to the classical fluid dynamic model noted above. This approach is based on Maxwell viscoelastic normal mode theory, i.e., a spectral method whereby the fields are expanded in spherical harmonics [*Peltier*, 1974; *Sabadini et al.*, 1982], and is particularly appropriate to investigate the effects of different wavelength components of surface deformation induced by any kind of source, thus also by internal density anomalies as done in the present study. Furthermore, the use of viscoelastic Maxwell Earth allows to decouple the pure elastic and the viscous contributions, thus allowing an important physical insight

[1]Dipartimento di Scienze della Terra, Sezione Geofisica, Università degli Studi di Milano, Milan, Italy.

0148-0227/06/2005JB003926$09.00

into the intimate dual nature, elastic and viscous, of our planet, for mantle density anomaly even on convection timescales.

[4] Use of viscoelastic Maxwell rheology is not a novelty in modeling the effects of mantle density anomalies. *Ricard and Sabadini* [1990] already pointed out the effects of Maxwell rheology on the buildup of geoid anomalies induced by redistribution of mass within the Earth in comparison with purely viscous models [*Richards and Hager*, 1984]. Viscoelastic Maxwell rheology has been used afterward for the interpretation of a variety of geophysical or geological observables, such as the displacement of the axis of rotation on timescales of hundred million years driven by subduction or upwelling plumes, as in work by *Spada et al.* [1992a] and *Greff-Lefftz* [2004], and eustatic sea level fluctuations induced by polar wander, as in work by *Sabadini et al.* [1990].

[5] LIPs are among the most important phenomena attributed to plumes, especially those from the mid-Cretaceous, a period characterized by some of the most anomalous events from a geological viewpoint. Increases in sea level of the order of 250 m with respect to the present-day level are certainly among the most sensational events to have occurred in that geologic era. The plumes hypothesized for LIP formation have been characterized well enough to serve as the basis of the present study via normal mode viscoelastic theory. We thus use plume terminology to indicate the superplumes rising from the deep part of the mantle, i.e., the core-mantle boundary (CMB).

[6] The hypothesis of the mid-Cretaceous superplume has been proposed by *Larson* [1991a, 1991b], and beyond the arguments in its favor, there have been criticisms such as those by *Hardebeck and Anderson* [1996]. Their argument is that the large oceanic crust production proposed by *Larson* [1991a, 1991b] together with the superswell caused by the superplume should have produced a eustatic sea level rise of about 470 m, the superswell contributing 220 m, which is inconsistent with the observed value of about 250 m. Thus, together with Earth's surface displacement caused by plumes, we want to evaluate also the global quantity called "eustatic sea level" (or eustasy) by *Hardebeck and Anderson* [1996]. On the basis of a simple reasoning, based on mass conservation principle, we can anticipate that the superswell caused by the superplume, cannot produce the large global sea level rise proposed by *Hardebeck and Anderson* [1996]. In fact, their estimate of global sea level rise accounts only for the volume forming the superswell itself, but that volume is made by material displaced from somewhere else in the Earth, necessarily producing a subsidence which compensates for the global sea level rise of the swell alone. An interesting question is thus where is that subsidence located and how large is it, focusing in particular on the influence of elastic lithospheric thickness and of dry land distribution over global sea level changes.

2. Earth Model

[7] The choice of Earth model is directly dependent on the kind of phenomena under study and on its mathematical tools and facilities. Since one of the final targets of the present analysis is the evaluation of sea level changes induced by mantle plumes, the spherical, self-gravitating, radially stratified viscoelastic Earth model, which is based on the linear Maxwell rheology and expanded in spherical harmonics, is the natural choice, thanks to the characteristics of these functions. The latter in fact self-consistently takes into account the effects of the elastic and viscous properties of the Earth for any kind of source on any of the three fields, namely vertical, horizontal displacements and gravity, in the near and in the far field, which in our analysis means at the antipodes with respect to the swell. These properties are fundamental for the evaluation of global quantities such as global sea level changes. Furthermore, the mathematical tools of normal mode expansion enable physical insight into the studied phenomena in terms of wavelengths, allowing to discriminate among the various spatial scales affecting the geophysical process under study.

2.1. Normal Mode Theory for Internal Density Anomalies

[8] The effects of mantle plumes are modeled by means of normal mode relaxation theory for an incompressible, stratified Earth. The explicit expression of the singular part of the Green function for spheroidal, incompressible deformation and gravitational perturbation, entering the fundamental matrix, necessary for modeling a multilayered Earth, has first been given by *Sabadini et al.* [1982], while the explicit expression for the inverse of the fundamental matrix, necessary for propagating the viscoelastic solution from the CMB to the Earth's surface, has first been given by *Spada et al.* [1990, 1992b]. Mathematical details for retrieving the fundamental matrix for stratified, viscoelastic Earth's models are given by *Sabadini and Vermeersen* [2004].

[9] Given the normal mode approach, the momentum and the Poisson equations for a Maxwell viscoelastic solid are expanded in spherical harmonics after the methodology of *Phinney and Burridge* [1973]. The Correspondence Principle is then applied to retrieve the viscoelastic solution in time domain. Similarly to the viscoelastic models used in the literature to model the effects of internal mass anomalies on geophysical observables [*Ricard and Sabadini*, 1990; *Spada et al.*, 1992a; *Greff-Lefftz*, 2004], our Earth model consists of four layers where the density and rigidity are specialized for an incompressible material (infinite bulk modulus) and volume averaged from PREM [*Dziewonski and Anderson*, 1981].

[10] Two lithospheric models are considered, with a 121- and 32.2-km elastic lithosphere, obtained by letting the viscosity $\nu \rightarrow \infty$ in the layer overlying an upper and a lower mantle, where the upper and lower mantle viscosities are fixed at 3.3×10^{20} and 10^{22} Pa s, respectively, and the core, as shown in Table 1. The 121-km lithospheric thickness is thus appropriate for modeling an average continental lithosphere as inferred by *Yuen et al.* [1983] from TPW and Length Of Day (LOD) variations on the basis of a four-layer viscoelastic model (as considered here). The 32.2-km lithospheric thickness, instead, is suitable for oceanic lithosphere, according to observations of flexure of oceanic lithosphere [*Watts*, 1978]. The lower mantle is thus 30 times more viscous than the upper mantle, in agreement not only with global geodynamic data, as in work by *Mitrovica and Forte* [2004] but also with Post-Glacial Rebound analyses, as in work by *James and Ivins* [1997] and *Tosi et al.* [2005]. In particular, we have used the same viscosity values as in

Table 1. Rheological Structure

Layer	r, km	ρ, kg/m^3	μ, Pa	ν, Pa
		Lithosphere Thickness 121 km		
1	6371	3234.0	5.99×10^{10}	1.0×10^{50}
2	6250	3631.0	8.60×10^{10}	3.3×10^{20}
3	5701	4878.0	2.17×10^{11}	1.0×10^{22}
4	3480	10,932.	0.00	0.0
		Lithosphere Thickness 32.2 km		
1	6371.0	2713.50	4.16072×10^{10}	1.0×10^{50}
2	6338.8	3601.03	8.60938×10^{10}	3.3×10^{20}
3	5701.0	4890.64	2.20957×10^{11}	1.0×10^{22}
4	3480.0	10,932.	0.00	0.0

Table 7 of *Tosi et al.* [2005], retrieved from inversion of mantle viscosities on the basis of Maxwell viscoelastic mantle rheology and long-wavelength, time varying gravity variations. Although identical to the four-layer viscoelastic models used in a series of previous studies in terms of parameter values, ours is based on exact integer algebra, as discussed in detail afterward, so as to secure the highest accuracy in the evaluation of Green functions.

[11] PREM volume average densities overestimate the density jump at 670 km depth at the upper-lower mantle interface, mainly affecting the slow M_1 mode, whose relaxation time is portrayed, for example, in Figure 2 of *Spada et al.* [1992b], a mode characterizing chemical interfaces, and not included in the modeling of phase-change interfaces [*Ricard and Sabadini*, 1990]. *Sabadini et al.* [1990] have shown, on the other hand, that for a viscously stratified mantle as considered here in agreement with *Mitrovica and Forte* [2004], *James and Ivins* [1997] and *Tosi et al.* [2005], the buoyant effect, and thus the strength, of the M_1 mode are offset by the viscosity hardening of the lower mantle, which makes chemical and phase-change interfaces to behave similarly and essentially to make our overestimation of the density jump at the upper-lower mantle interface ineffective.

[12] Both chemical and phase-change interfaces here are considered at the upper-lower mantle boundary at 670 km depth. Chemical boundary includes the M_1 mode excited by the density discontinuity at 670 km, while in the phase-change interface this mode is not included: the M_1 mode inhibits displacement of the 670 km interface and thus mimics the behavior of a chemical boundary where no material crosses, while deleting the M_1 mode simulates a phase-change boundary, where material does cross the boundary. Including or deleting the M_1 mode is the usual way of simulating chemical and phase-change interfaces in viscoelastic normal mode theory, when the realistic kinetics of the 670 km interface cannot be fully exploited [*Ricard and Sabadini*, 1990; *Sabadini et al.*, 2002].

[13] Our analytical treatment requires a laterally homogeneous Earth model and thus the spheroidal solution, which is the only one to be dealt with for internal loading, does not contain any longitudinal component. The radial and tangential displacement components and the perturbation of the gravitational potential are then expanded in Legendre polynomials $P_\ell(\cos\theta)$ rather than in spherical harmonics. The radial and tangential displacement components u and v and the perturbation in the gravitational potential ϕ_1, as functions of the scalars U_ℓ, V_ℓ and $\phi_{1,\ell}$, which depend on the harmonic degree ℓ and on the radial distance r_s of the source from the center of the Earth, are thus given as a function of the Love numbers h_ℓ, l_ℓ and k_ℓ,

$$\begin{bmatrix} U_\ell \\ V_\ell \\ \phi_{1,\ell} \end{bmatrix} = \frac{\phi_{2,\ell}}{g} \begin{bmatrix} h_\ell \\ l_\ell \\ k_\ell\, g \end{bmatrix}, \tag{1}$$

where g is the gravity acceleration evaluated on the surface of the Earth.

[14] The harmonic coefficients of the perturbing potential ϕ_2 are

$$\phi_{2,\ell}(r_s) = \frac{a\, g}{M_T} \left(\frac{r_s}{a}\right)^\ell, \tag{2}$$

and if the perturbed potential ϕ_ℓ denotes the total potential $\phi_1 + \phi_2$, by introducing the generalized Love numbers defined as follows, we have

$$\begin{bmatrix} U_\ell(r_s) \\ V_\ell(r_s) \\ \phi_\ell(r_s) \end{bmatrix} = \frac{a}{M_T} \begin{bmatrix} h_\ell(r_s) \\ l_\ell(r_s) \\ k_\ell(r_s) g \end{bmatrix}, \tag{3}$$

where $h_\ell(r_s)$, $l_\ell(r_s)$ and $k_\ell(r_s)$ are now defined according to the previous three equations, and M_T and a are the mass and the radius of the Earth, respectively. We should remind that the quantities U_ℓ, V_ℓ and ϕ_ℓ are defined for a unitary mass, i.e., the point-like source.

[15] Application of the residue theorem to evaluate the inverse Laplace transform from the s-domain to the time domain results into the solution for the fields U_ℓ, V_ℓ and ϕ_ℓ at the surface of the Earth. The Love number pertaining to the radial displacement becomes

$$h_\ell(r_s, t) = h_{\ell e}(r_s)\delta(t) + \sum_{j=1}^{M} h_{\ell j}(r_s)\, e^{s_j t}, \tag{4}$$

where s_j are the inverse relaxation times and r_s is the radial distance of the source.

2.2. Rising Density Anomaly

[16] A column of density anomaly, as sketched in Figure 1, grows in time according to the law of motion $r_s(t)$, with r_s denoting the depth of the density anomaly as a function of time, from the core-mantle interface R_0 to the lithosphere-mantle interface R_1. This column is built up by thin contributions of thickness $dr_s(\tau)$ which, once excited, remain constant in time, as described by the Heaviside function, and are excited one after the other according to the law of motion $r_s(t)$. The convolution in time of the Green function (equation (4)) with the Heaviside function gives the following harmonic coefficients for a point-like density anomaly,

$$h_{\ell r_s}(t) = \left(h_e(r_s(\tau)) - \sum_j \frac{h_j(r_s(\tau))}{s_j} \left(1 - e^{s_j(t-\tau)}\right) \right) H(t-\tau). \tag{5}$$

[17] The harmonic coefficients for the vertical displacement for a rising column in dimensionless form is then

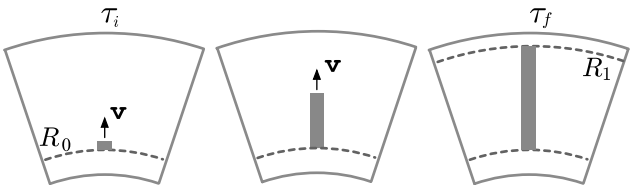

Figure 1. Sketch of three stages of the rising column at velocity v, leaving the CMB, denoted by R_0, at τ_i, and reaching the bottom of the lithosphere denoted by R_1 at τ_f.

obtained by integrating over $r_s(\tau)$ between an initial and a final time τ_i and τ_f so that $r_s(\tau_i) = R_0$ and $r_s(\tau_f) = R_1$. If the dependence on τ is all in $r_s(\tau)$, for example, in the first addendum in equation (5), it is convenient to integrate over r between R_0 and R_1, otherwise it is easier to explicit the dependence on τ and integrate over τ, so we obtain

$$[h_\ell](t) = \int_{R_0}^{R_1} \left(h_e[r] + \sum_j \frac{h_j[r]}{s_j} \right) H(r_s(t) - r)\mathrm{d}r + \int_{\tau_i}^{\tau_f} \sum_j \frac{h_j[r_s(\tau)]}{s_j} e^{s_j(t-\tau)} H(t-\tau)\, \dot{r}_s(\tau)\mathrm{d}\tau, \quad (6)$$

where the dot denotes the time derivative and the two contributions, from the fluid or steady state limit and from the transient part containing the decaying exponentials, have been separated and in the second integral the time dependence is left explicit. If the first integral in equation (6) is indicated by $[h_\ell]^F(t)$ and the second integral by $[h_\ell]^T(t)$, the function for the rising anomaly can be shortly written as

$$[h_\ell](t) = [h_\ell]^F(t) + [h_\ell]^T(t). \quad (7)$$

[18] Notice that, analyzing the first integral in equation (6), the amplitude of the fluid part $[h_\ell]^F(t)$ is unaffected by the law of motion $r_s(t)$ or by the velocity law $\dot{r}_s(t)$. In fact, by defining $p := r_s(t)$, the integral function $[h_\ell]^F(t)$ can be written as a parametric function as follows:

$$[h_\ell]^F(t) = \begin{cases} p = r_s(t) \\ [h_\ell]^F(p) \end{cases},$$

where $[h_\ell]^F(p)$ is a function of the position p, and the function $r_s(t)$ controls only the dilatation of the function on the t axis.

[19] On the contrary, the amplitude of the transient part $[h_\ell]^T(t)$ depends on $\dot{r}_s(t)$ which is a velocity (constant or variable), considered positive. Replacing the function $\dot{r}_s(t)$ by its maximum $v_{\max}$, it is easy to see that the new function $[h_\ell]^T(t)$ is always greater than the previous one, and this makes the maximum of the transient term roughly linearly dependent on the maximum of the rising velocity. Furthermore, when the maximum velocity $v_{\max}$ of the rising anomaly is below 10–15 cm/yr, it is possible to demonstrate, from the mathematical standpoint and from the findings in Figure 5 in section 4.3, as discussed below, that under the considered conditions the transient term $[h_\ell]^T(t)$ is negligible with respect to the fluid one $[h_\ell]^F(t)$.

[20] Thus it is possible to simplify the problem by neglecting the transient part, and so the dependence on velocity $\dot{r}_s(t)$. These results are used in the following section to simplify the plume model.

3. Plume Model

[21] The well-known idea of a plume with mushroom-shaped head and conduit has been inspired by experiments, such as the injection of low viscosity fluid at the base of a viscous fluid [*Griffiths and Campbell*, 1990; *Kumagai*, 2002], even though it is possible to reproduce the head and conduit by numerical simulations [*Van Keken*, 1997]. Another kind of experiment is based on the localized fusion of crystalized bodies [*Kirdyashkin et al.*, 1987]. In these experiments the head and the conduit are not observed. These characteristics are thus sufficiently relevant to discriminate among the various plume shapes and hypotheses and may be helpful for the interpretation of seismic tomography images; the missing head and conduit in the mantle regions where the plumes have been hypothesized, could be ascribed to insufficient resolution of seismic tomography.

[22] The driving force of hot rising plumes is thermal buoyancy but phase changes modify the material of the mantle, thereby affecting buoyancy. *Marquart et al.* [2000] focus on the temperature and dimension that must characterize the plume so that it can cross the thermal interface, concluding that the radius has to be larger than about 100 km and the temperature contrasts have to be larger than 400°C; the highest rising velocity is about 14 cm/yr, being reduced to 3 cm/yr at the interface. *Richards et al.* [1989] suggested that most LIPs are due to rapid melting of the plume head, and *Coffin and Eldholm* [1993] estimated the mantle volume necessary to generate many of them. For instance, for the Ontong Java Plateau, the plume radius has been estimated as between 350–600 km.

[23] While *White and McKenzie* [1989] suggested for large thermal anomalies underneath the lithosphere plume radii of the order of 2000 km, the head of the anomaly should be considered as squeezing and widening with respect to the effective spherical radius of about 300 km. *Griffiths and Campbell* [1990] also suggested large plumes, studying the transport properties within the plumes in laboratory experiments and concluding that the plume's head should have a radius of the order of 500 km when it hits the upper mantle; the transport properties, on the other hand, critically depend on how the plume is formed, i.e., whether it originates at the thermal interface or it has been created by injection of matter [*Van Keken*, 1997]. Numerical experiments using 2-D cylinders for plumes from the thermal interface show that the effective radius should be of the order of 120–170 km for Rayleigh numbers of the order of 4.4×10^7–5×10^6 [*Van Keken*, 1997]. The dimensions of laboratory and numerically generated plumes thus depend on the conditions of the mantle layers, although it is generally agreed that LIPs are generated by large plumes with effective radii larger than 200 km.

[24] As anticipated, another important parameter is the excess temperature, which *Schilling* [1991] estimated from petrology and geochemistry to be of the order of 250°C.

While Hawaii numerical models indicate an excess temperature of 280°C [*Watson and McKenzie*, 1991], dynamic models of the plume-lithosphere interaction show that plume head excess temperature would be 350°C [*Farnetani and Richards*, 1994].

[25] For surface uplift, *Farnetani and Richards* [1994] evaluated the vertical displacement (of the surface) over the plume, as modeled by a sphere characterized by an initial radius of 400 km and an excess temperature of 350°C, and they came up with a vertical displacement range of 2–4 km. *Griffiths and Campbell* [1991], working on larger plumes, obtained a smaller swell of about 600 m.

[26] Other studies have focused on the bulge induced on the lithosphere by more general internal mass heterogeneities, rather than plumes, such as the large topography excess over Africa [*Gurnis et al.*, 2000; *Lithgow-Bertelloni and Silver*, 1998]. From lower mantle density contrasts inferred from seismic tomography, *Gurnis et al.* [2000] estimate the surface uplift to be of the order of 1 km, on the basis of the rate of uplift. Furthermore, *Forte and Woodward* [1997], from the global viscous flow driven by the seismically inferred mantle density anomalies, estimated a dynamic topography of 2 km at most, at long wavelengths from harmonic degree $\ell = 1$ to $\ell = 8$.

[27] Given the absence of a clear definition of plume and of its variety of shape and dimension, it seems plausible to build as simple a plume model as possible, for example a sphere to simulate the head and an underlying column to simulate the conduit. This approach has been taken in several fluid dynamic and true polar wander simulations [*Gurnis et al.*, 2000; *Greff-Lefftz*, 2004]. Yet since our main goal is to evaluate the global effects induced by plumes, rather than the detail of the surface deformation patterns, modeling the plume head by means of a cylinder has been preferred to the sphere because it is simpler from the mathematical point of view. Furthermore, in order to compare the results with other simulations in the literature, the volume of the cylinder is taken as that of the equivalent sphere, so that the radius of the cylinder is identical to the sphere's and its height is four thirds of the radius'. We employ three shapes in our final analysis: a cylinder for the plume head, a column for the conduit and the combination of the two.

[28] The thermal expansion coefficient varies between $\alpha = 2.5 \times 10^{-5}$ and $\alpha = 3 \times 10^{-5}$ K^{-1}. As noted above, the excess temperature ΔT of the plume ranges between 250 a 350°C. If ρ_0 denotes the background density, the density contrast is given by

$$\Delta\rho = -\rho_0 \alpha \Delta T. \tag{8}$$

[29] The density contrast is chosen by fixing $\alpha\Delta T = 10^{-2}$, which corresponds to a 330–400°C temperature range and to a thermal expansion coefficient varying as previously specified. The density contrast agrees, for example, with that inferred from seismic tomography, varying between −1 and +1% with respect to the background density [*Gurnis et al.*, 2000].

[30] A plume which leaves the core-mantle interface and reaches the base of the lithosphere, crosses the two different densities of the lower and upper mantle. The mass of the anomaly is assumed to remain constant when passing through the lower-upper mantle interface, implying that

$$\rho_2 A_2 \mathrm{d}r = \rho_3 A_3 \mathrm{d}r, \tag{9}$$

i.e., in the lower mantle (layer 3 with density ρ_3) an infinitesimal portion of the column (or cylinder) of area A_3 and thickness dr conserves its mass when it enters the upper mantle (layer 2 with density ρ_2).

[31] The results of the present analysis will be compared to those of *Farnetani and Richards* [1994], who employed a sphere with an initial radius of 400 km. This means that in our simulation the cylinder has a radius of 460 km while it is crossing the uppermost layer, with height of $h = 613$ km. A column with 300 km radius will also be treated, together with a cylinder having a 300 km radius overlying a conduit with a 100 km radius, the ratio thus being one third.

[32] The plume in our analysis will cross the upper-lower mantle interface, which is modeled by means of both a chemical and phase-change boundaries: chemical interface does not allow the mantle material to cross the boundary, while the phase-change does. The superplume acts on the timescale of tens of millions of year and, being such a slow process, it is reasonable to consider the phase-change interface for the superplume simulation; both interfaces are considered first, focusing on phase-change upper-lower mantle interface in the final simulations.

[33] The plume's rising velocity is treated as a kinematic condition and, although it is not constant when, for example, the anomaly is crossing the upper-lower mantle interface at 670 km depth, as shown by *Marquart et al.* [2000], we assume it as constant on the basis of the considerations above. In fact, we have shown in the previous section that the rising velocity controls only the duration of the process, namely the dilatation of the t axes.

4. Evaluation of the Green Functions for Internal Loads

[34] In order to retrieve an analytical expression of the harmonic coefficients as a function of source depth, a symbolic manipulator is used to make the analytical evaluation of the integrals in equation (6) easier. Furthermore, in order to avoid any problem due to numerical instability caused by stiffness of the fundamental matrix for stratified, viscoelastic, incompressible Earth, first defined by *Sabadini et al.* [1982], all the calculations are based on exact integer numbers so as to secure the highest accuracy until the very end of the calculations, when they are approximated to real numbers or when the roots and residues are evaluated. Stiffness is due the regular and singular parts of the fundamental matrix, necessary for evaluating the viscoelastic solution, behaving as $(r/a)^{\ell}$ and $(r/a)^{-\ell}$ for $\ell \to \infty$, where a is the Earth's radius and ℓ is the harmonic degree. Since the radii r where interfaces are located are smaller than the Earth's radius, $(r/a)^{\ell} \to 0$ and $(r/a)^{-\ell} \to \infty$ in the evaluation of the viscoelastic solution, we have to cope with differences between extremely small and extremely large numbers. Details on the behavior of the fundamental matrix and on the technique to avoid such numerical difficulties are discussed by *Riva and Vermeersen* [2002]. Although the technique proposed by *Riva and Vermeersen* [2002] has not

been applied in our analysis, our final results are not affected by inaccuracies, thanks to the use of integer algebra.

[35] Matrix propagation from CMB up to Earth's surface and evaluation of secular determinant for evaluation of inverse relaxation times are carried on by means of symbolic calculus. Green function are then obtained as explicit functions of depth source r_s, thus allowing to derive analytical expressions for the integral functions given by equations (12) and (13) in the following. Plume upwelling is in this way modeled by means of continuous, not step-like, functions in time.

4.1. Fluid Limit for Internal Loads

[36] It is necessary to estimate the number of spherical harmonics that must be summed up for convergence of the solution. In principle, any geophysical process requires that a characteristic harmonic degree ℓ is reached in the expansion so as to ensure that the solution is accurate enough. For example, use of normal mode theory to evaluate the coseismic displacement for shallow earthquakes requires summation over 40,000 spherical harmonics, while for post-seismic deformation from the same source summation over 3000 harmonics is appropriate [*Dalla Via et al.*, 2005]. Reconstruction of the geophysical observable associated with post-glacial rebound, and thus redistribution of surface loads, requires summation over about 150 spherical harmonics [*Mitrovica and Peltier*, 1989]. This usually depends on the dimensions of the source load, but we show that this also depends on the trend of the harmonic coefficients of the Green functions with the harmonic degree. In order to estimate the truncation level, and thus the highest spherical harmonic degree for the present problem associated with internal loads, the fluid limit for $t = \infty$, given by the following expression:

$$h_f = h_e(r_s) - \sum_j \frac{h_j(r_s)}{s_j} \tag{10}$$

is considered, which includes the elastic and viscous contribution h^E, h^V, according to

$$h^E(r_s) = h_e(r_s) \quad \text{and} \quad h^V(r_s) = \sum_j \frac{h_j(r_s)}{s_j}. \tag{11}$$

We note that elasticity, through h^E, enters the fluid (or steady state) limit of the Green functions, simply reflecting the intimate nature of the mechanical behavior of the entire Earth, including mantle and lithosphere, which behaves simultaneously as an elastic and viscous material, as appropriately modeled by viscoelasticity.

[37] For surface loads, *Le Meur and Hindmarsh* [2000] analyzed the Gibbs phenomenon and the methodology to be applied to overcome its effects due to truncation of the series. Following their procedure, we evaluate the spherical harmonic coefficients of the surface vertical displacement in dimensionless form up to the harmonic degree $\ell = 100$, as a function of the load depth within the mantle, the lithosphere and at the Earth's surface. Both cases of phase-change and chemical interfaces between the upper and lower mantle, which affect solely the viscous response, are taken into account.

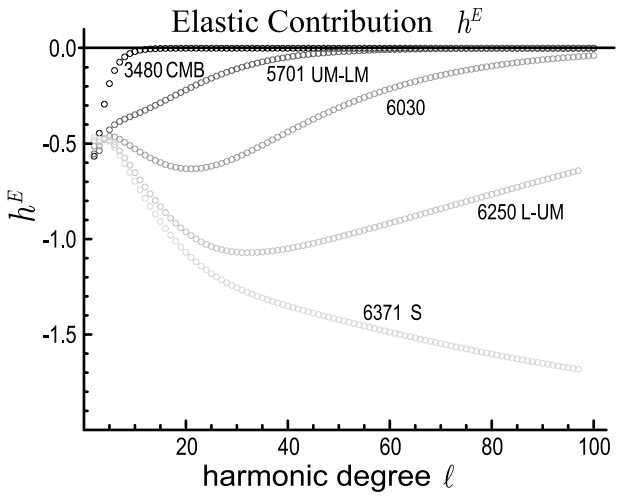

Figure 2. Elastic component h^E as function of the harmonic degree ℓ, evaluated for a unitary load embedded at the Earth surface S at 6371 km, at the lithosphere–upper mantle interface L-UM at 6250 km, at 6030 km, at the upper-lower mantle interface UM-LM at 5701 km, and at the CMB at 3480 km.

[38] As anticipated by *Farrel* [1972], *Le Meur and Hindmarsh* [2000] show that the major problem with the truncation is the elastic contribution. In fact, for surface loads it tends asymptotically, for increasing ℓ, to a nonvanishing negative value (their Figure 3), while the viscous contribution for chemical interface tends to zero (their Figure 2).

[39] Figure 2 shows the elastic contribution of the fluid limit as a function of the harmonic degree ℓ, for embedded loads with depth ranging from the Earth's surface, corresponding to the 6371 S case, light gray, to the core-lower mantle boundary, 3480 CMB case, black dots. Both elastic (light gray dotted curve in Figure 2) and viscous contributions for surface loads evaluated within our scheme for a chemical interface agree with the findings of *Le Meur and Hindmarsh* [2000] (their Figures 2 and 3), which confirms the validity of the methodology used in the present study.

[40] This means that for a surface load the truncation problem is driven by the harmonic coefficient of the load, i.e., the smaller is the load and the higher is the truncation degree. For the internal load, instead, we show that the truncation problem is driven only by the intimate behavior of the Earth, i.e., the harmonic coefficient of the Green functions and in particular of its elastic contribution.

[41] In fact, increasing the depth of the source makes the elastic contribution tend to zero with increasing ℓ, as Figure 2 shows. For loads embedded at the upper-lower mantle interface (5701 UM-LM case) the elastic contribution after $\ell = 60$ is almost negligible, and at the CMB it vanishes for very low degrees, namely after $\ell = 10$. Although it is not shown here, we obtain also that the viscous contribution tends to zero for increasing ℓ not only for surface loads but also for deep ones, and much faster than the elastic contribution.

[42] The behavior of both the viscous and the elastic contribution means that increasing the depth of the source

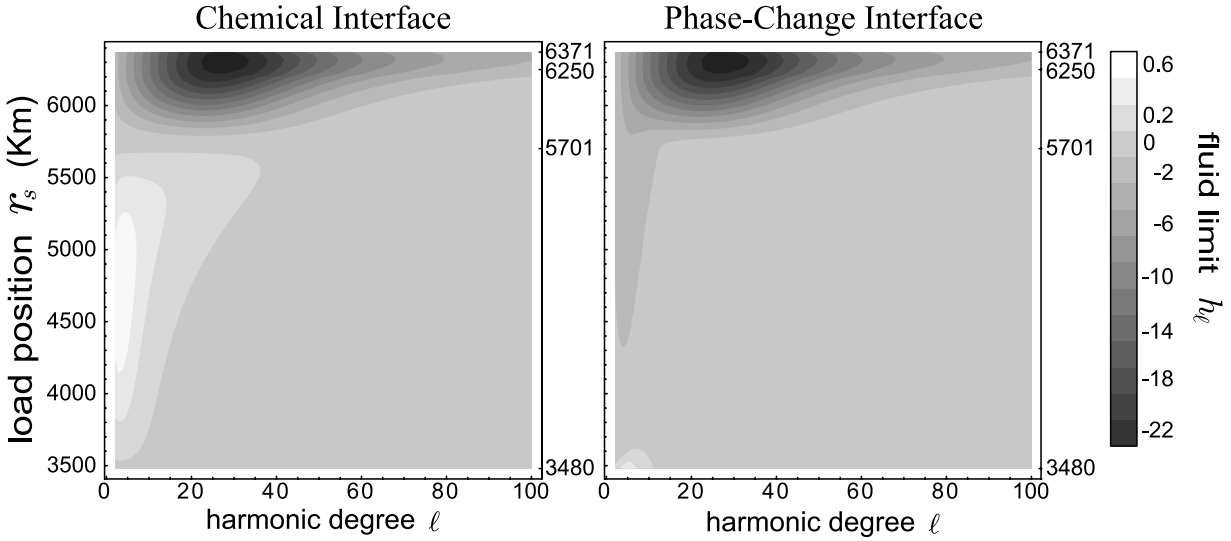

Figure 3. Fluid limit h_ℓ as a function of the harmonic degree ℓ, horizontal scale, and load position r_s in kilometers, from the CMB at 3480 km to the Earth surface at 6371 km, for (left) chemical and (right) phase-change interface. The radius of the lithosphere–upper mantle and upper-lower mantle interfaces, at 6250 and 5701 km, are also provided. Values are based on the vertical gray scale on the right.

makes the portion of the Earth overlying the source acting as a low-pass filter, with the details of the load being increasingly filtered out with depth. The same behavior can easily be seen in the fluid limit h_f in Figure 3, which provides a global view of the dependence of the fluid limit h_f as a function of the radial distance of the density anomaly r_s, vertical axis, and harmonic degree ℓ, horizontal axis; the left panel stands for a chemical interface and the right one for a phase-change interface. The darker the gray, the negatively larger is the amplitude of h_f, as shown by the dark spots between the surface and depths of about 400 km, or radial distance of 6000 km, and harmonic degrees varying between $\ell = 10$ and $\ell = 60$, indicating that the effects on the vertical displacement is the largest for density anomalies embedded in the upper mantle, for both chemical and phase-change interfaces. This means that even at shallow source depths, the portion of the Earth overlying the source acts as a low-pass filter and contributions for ℓ higher than 60 are negligible. For a chemical interface, we note the change in sign of the fluid limit h_f in the lower mantle, due to the buoyant chemical boundary which, being harder to displace than a phase-change interface, decouples the mantle, with sources located in the upper and lower mantle affecting in a different fashion the displacement at the Earth's surface.

4.2. Integral Functions

[43] The dimensionless function $[h_\ell](p)$, with $p := p(t)$ denoting the top of the columns, contains the fluid and the transient parts, indicated by $[h_\ell]^F$ and $[h_\ell]^T$, respectively. The fluid part contains the elastic and viscous contributions, indicated by $[h_\ell]^E$ and $[h_\ell]^V$, respectively. For p varying between the CMB and the lithosphere-upper mantle interface, the elastic and viscous parts are

$$[h_\ell]^E(p) = \int_{R_0}^{p} h_e[r_s]\mathrm{d}r_s \tag{12}$$

$$[h_\ell]^V(p) = \int_{R_0}^{p} \sum_j \frac{h_j[r_s]}{s_j}\,\mathrm{d}r_s. \tag{13}$$

As functions of the depth of the top of the column p, Figure 4 shows the integral functions $[h_\ell]^V$ and $[h_\ell]^E$.

[44] With respect to h_ℓ^E and h_ℓ^V portrayed in Figures 2 and 3, the decay for increasing harmonic degree ℓ is even more pronounced for these integral functions, thus justifying the truncation at $\ell = 100$ in the spherical harmonic expansion. The values of these integral functions are generally lower than the Love numbers of Figure 3 since they are integrated over the normalized r variable, which is always smaller than unity. Figures 2–4 clearly show the low-pass filter properties of the portion of the Earth overlying the source, which justifies the choice of simple plume shapes in our simulations and the attention drawn on other important plume properties, such as mass and dimension.

4.3. Deleting the Transient Contribution

[45] The radial displacement $U(t, \bar{r}, \theta)$ for a rising column is given by the convolution of the Green functions, the generalized Love numbers as defined in equation (3), with the load function. This convolution has been described in the previous section 2.2 and, with $\Delta\rho$ of the plume as given in equation (8), by summing over ℓ, $U(t, \bar{r}, \theta)$ can be expressed by

$$U(t,\bar{r},\theta) = \frac{a}{M_T}\,\Delta\rho\, A_c \sum_\ell P_\ell(\cos\theta)\Big([h_\ell]^F(t,\bar{r}) + [h_\ell]^T(t,\bar{r})\Big), \tag{14}$$

where A_c is the area of the cross section as a function of the base radius and where the expression for the radially rising column, equation (7) is modified so as to account

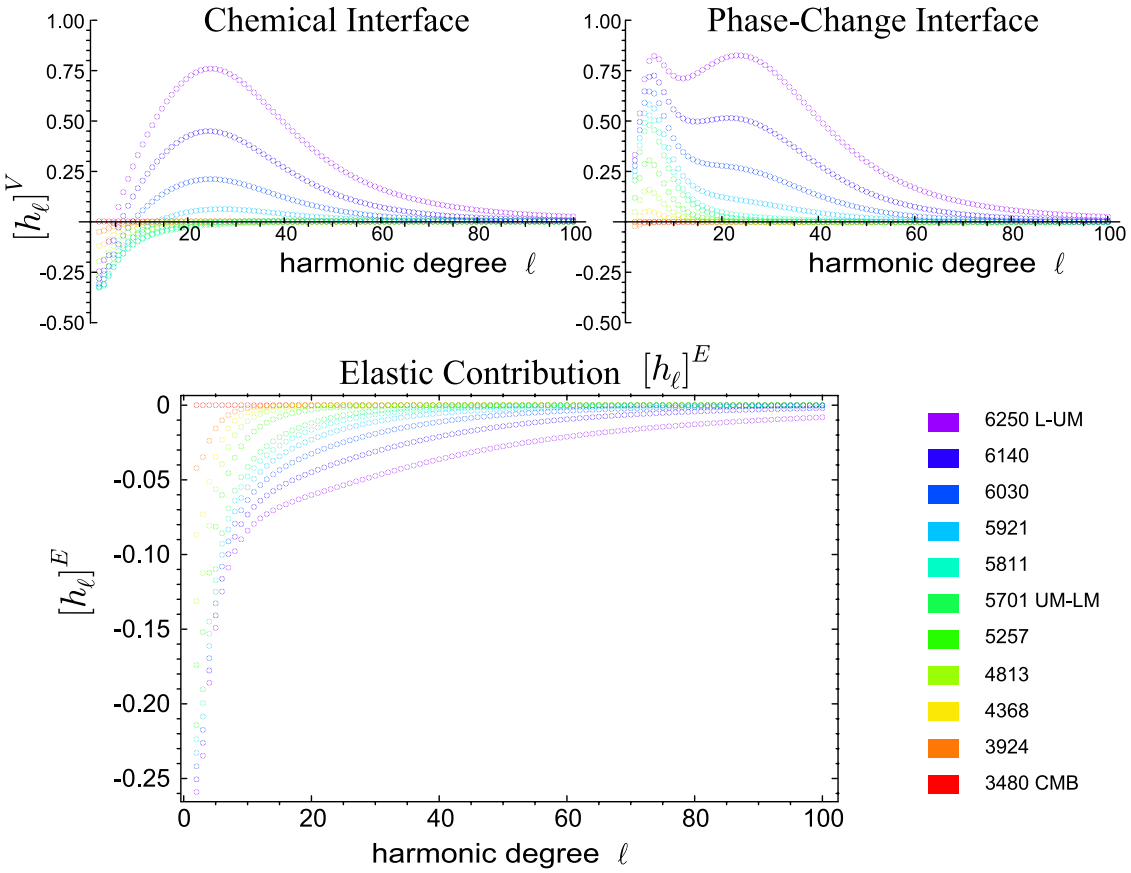

Figure 4. (top) The $[h_\ell]^V$ as a function of the harmonic degree ℓ, when the top of the dimensionless column is located at different radial distances, i.e., from the CMB, at 3480 km (red), the upper-lower mantle interface UM-LM (green), and up to lithosphere-upper mantle interface L-M at 6250 km (violet). (left) A chemical interface. (right) A phase-change interface. (bottom) From the lithosphere to the CMB, showing the elastic term $[h_\ell]^E$. Radius is given in kilometers. Lithospheric thickness is fixed at 121 km.

for the disk coefficients (for unit mass) [*Farrel*, 1972] arranged in the following form

$$L_\ell(r_s,\bar{r}) = \frac{2}{\ell(\ell+1)}\left(1-\frac{\bar{r}^2}{4r_s^2}\right)P'_\ell(x) \quad \text{with} \quad x = 1-\frac{\bar{r}^2}{2r_s^2}, \quad (15)$$

where $P'_\ell(x)$ is the derivative with respect to x of the Legendre Polynomial, $\bar{r}$ is the base radius of the column and r_s is the radial distance of the top of the column; it is quite evident that if $\bar{r} \to 0$ then $L_\ell \to 1$ holds. $U(t, \bar{r}, \theta)$ can be written in compact form, as the sum of the fluid and transient part,

$$U(t,\bar{r},\theta) = A_c\left(\overline{U}^F(t,\bar{r},\theta) + \overline{U}^T(t,\bar{r},\theta)\right), \quad (16)$$

where the term $A_c := A_c(\bar{r})$ is a function of the base radius, but it is useful to set it to a constant unitary area $A_c = \pi 10^2$ km^2, as will be made clear afterward.

[46] In order to compare the fluid and transient contributions to the vertical displacement $U(t, \bar{r}, \theta)$, Figure 5 portrays the complete solution obtained by summing the harmonic terms from $\ell = 2$ to $\ell = 100$ for a column made of point-like sources ($\bar{r} = 0$ or $L_\ell = 1$), from $t = 0$ to $t = 60$ Myr, and A_c set to the unitary area. We choose the column made of point-like sources ($\bar{r} = 0$ or $L_\ell = 1$), since this case is the most favorable one for the transient part, the latter being in all the other cases with $\bar{r} > 0$ or $\|L_\ell\| < 1$ always smaller than the $\bar{r} = 0$ case, as it can be easily obtained from the above equation (15).

[47] The top row refers to the fluid contribution and the bottom one to the transient contribution; two upwelling velocities v_1 and v_2 are considered of 0.1 m/yr and 0.05 m/yr, solid and dashed lines respectively. The value of the displacement is evaluated at the Earth's surface and on the top of the upwelling density anomaly at $\theta = 0$ with respect to the source, where the deformation is the largest. The left column stands for a chemical boundary at the upper-lower mantle interface and the right for a phase-change interface.

[48] Figure 5 shows that the slowest velocity is responsible for the delayed vertical displacement of the surface, as expected, without changes in the amplitude. The maximum displacement of the transient part is about directly proportional to the upwelling velocity, as anticipated in previous section.

[49] Another important aspect of Figure 5 is the different behavior of the chemical and phase-change interfaces, the former being responsible for a vertical displacement that, in the final stage, is about 30 percent lower than the one corresponding to the phase-change interface. For a time

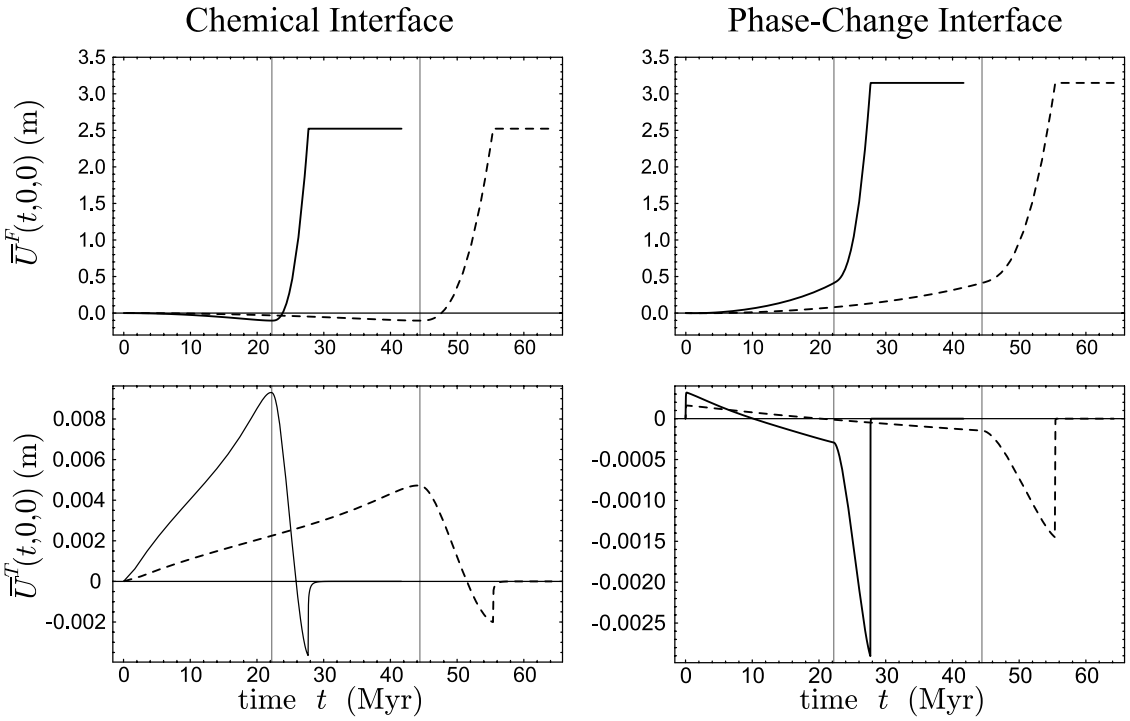

Figure 5. Time evolution of the radial displacement at $\theta = 0$, in terms of (top row) the fluid part $\overline{U}^F$ (t, 0, 0), and (bottom row) transient part $\overline{U}^T$ (t, 0, 0), for unitary area (m/(π 100 km^2)), for an infinitely thin column. Time $t = 0$ corresponds to the beginning of the process. Solid curves stand for a rising velocity $v = 0.1$ m/yr and dashed ones for $v = 0.05$ m/yr.

span of about two thirds of the entire time evolution, a lowering rather than uplift of the crust is predicted by chemical interface. This behavior of the chemical boundary is clearly due to its ability to damp the flow in the mantle and to decouple the circulation in the upper and lower mantle, from which even a change of sign in the surface displacement can be produced.

[50] From the bottom rows, referring to the purely transient part, we note that the latter is negligible with respect to the fluid part when the anomaly crosses the upper mantle, right of vertical gray lines. In the lower mantle, this conclusion always holds for phase-change interface, while for the chemical case, the transient part is of the order of 10–20% of the fluid part. Bearing in mind that this percentage is drastically reduced for realistic plume radii and that most of the lithospheric swelling builds up when the anomaly crosses the upper mantle, we neglect in the following the transient part of the solution. Velocity of the rising material clearly does not affects the amplitude of the surface deformation, but determines the time duration of plume upwelling, from the CMB to the bottom of the lithosphere.

5. Time Evolution of the Radial Displacement

[51] For two lithospheric thicknesses of 121 and 32.2 km, this section is devoted to the analysis of the radial, or vertical, displacement induced at the Earth's surface by a column and by a cylinder that rise at the same constant velocity $v = 10$ cm/yr, from the CMB up to the lithosphere-upper mantle interface. This vertical displacement is a dynamic topography of the Earth surface supported by the mantle viscoelastic flow driven by the density anomaly.

[52] The column stops rising when its top hits the lithosphere-upper mantle interface, after which the density anomaly remains constant. Unlike the column, the cylinder grows at the CMB until it reaches a specified thickness, after which it detaches from the CMB and moves upward until it hits the lithosphere-upper mantle interface, and, for the sake of simplicity, disappearing thereafter although in more realistic simulations the plume head would spread beneath the lithosphere. The density contrast $\Delta\rho$ is fixed at the same value for both the column and the cylinder; the cylinder is appropriate for analyzing the effects of the plume head and the column those of the plume conduit.

[53] In Figure 6, left column stands for chemical interface, right one for phase-change interface; lithospheric thickness is fixed at 121 km for the first and second row and at 32.2 km for the third and fourth rows. First and third rows correspond to columns while second and fourth rows to cylinders.

5.1. Influence of the Shape of the Load on the Earth Surface Response

[54] In order to estimate the impact of the shape of the density anomaly on the radial displacement, it is useful to evaluate the $\overline{U}(t, \bar{r}, \theta)$ surface displacement caused by the column in terms of the unitary cross-sectional area of π 100 km^2, as anticipated in the previous section. This means that while the area A_c is a factor which pertains to the dimensions, the $\overline{U}(t, \bar{r}, \theta)$ dependence on the shape is contained, inside the integral $[h_\ell]^F(t, \bar{r})$, within the load

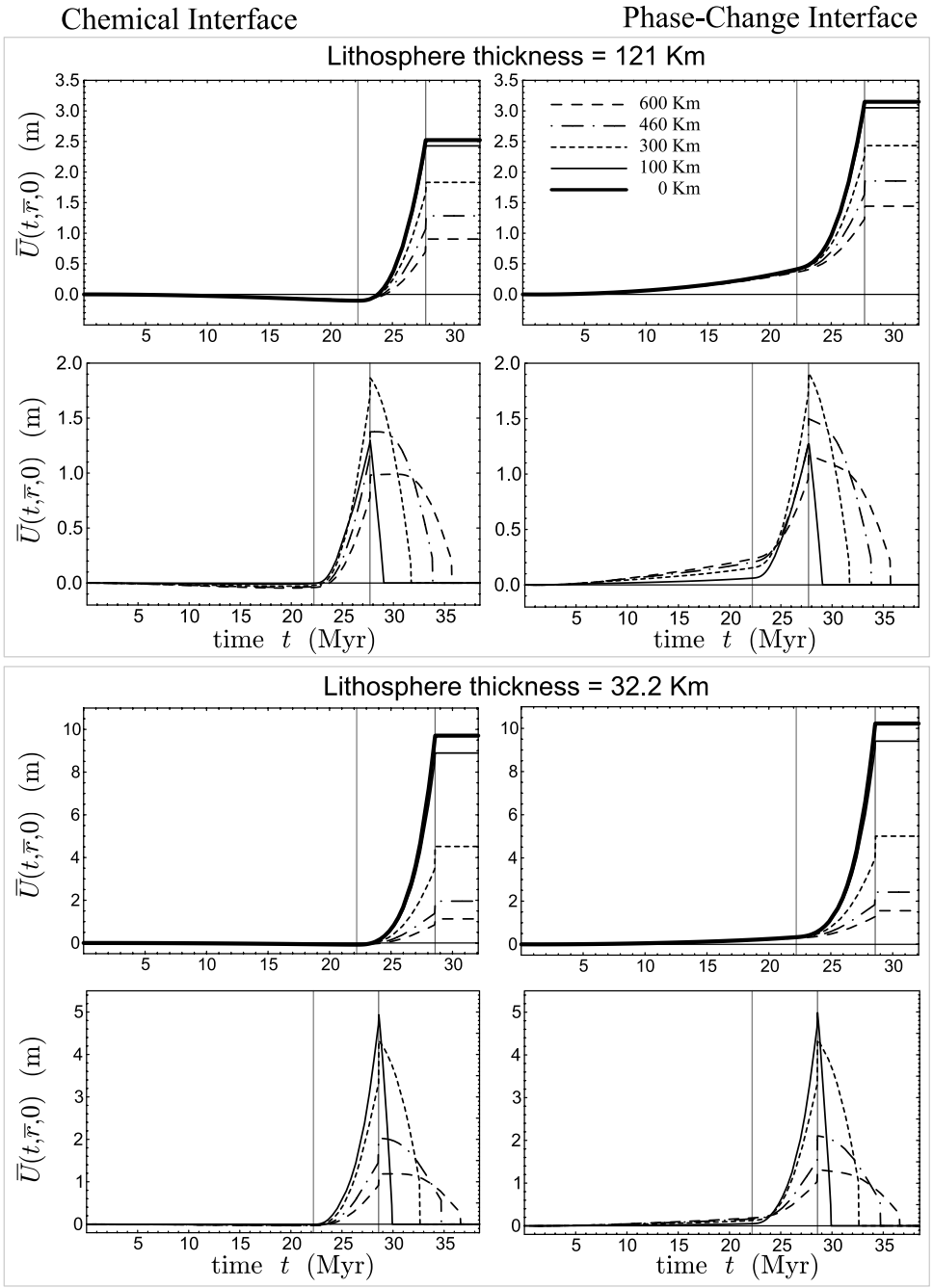

Figure 6. Time evolution of the radial displacement $\overline{U}(t, 0, 0)$ at $\theta = 0$ for unitary area (m/(π 100 km^2)), for columns, first and third rows, and cylinders, second and fourth rows, characterized by base radii from 100 to 600 km, as specified in the insets. Thick solid line stands for an infinitely thin column. The first and second rows correspond to a lithospheric thickness of 121 km, while the third and fourth rows correspond to a lithospheric thickness of 32.2 km. The vertical line between 20 and 25 Myr indicates the crossing of the upper-lower mantle interface. The plume head hits the bottom of the lithosphere at 28 Myr, as shown by the second vertical line on the right.

coefficients $L_\ell(r_s, \overline{r})$ (equation (15)). As anticipated, the height of the cylinders used for the bottom panels is four thirds of the base radius. The solution $U(t, \overline{r}, \theta)$ for the cylinder can be obtained by the composition of two columns as

$$U(t,\overline{r},\theta) = U(t,\overline{r},\theta)H(t) - U(t-\Delta\tau,\overline{r},\theta)H(t-\Delta\tau), \quad (17)$$

with $\Delta\tau = (4/3)\,\overline{r}/v$ and $H(t)$ being the Heaviside function.

[55] Thus Figure 6 shows the radial displacement at the Earth surface on the top of the anomaly ($\theta = 0$), for columns and cylinders of varying cross-sectional radius $\overline{r}$: for the column, the case of an infinitely small radius is also considered (solid line), which is the same as in Figure 5. The radius of the anomalies varies from 100 to 600 km, as given in the insets, so that the results must be multiplied by the factor $\overline{r}^2/10^2$.

[56] For a lithospheric thickness of 121 km, first and second rows, the vertical displacement of the Earth's surface varies from hundred meters (for example, cylinder and chemical or phase-change interface, solid curve: $\sim$1.3 ($100^2/10^2$) $\approx$ 130 m) to kilometers (e.g., column and phase-change interface, dashed curve: $\sim$1.5 ($600^2/10^2$) $\approx$ 5400 m). The trend of the functions for the chemical and phase-change interfaces portrays a similar pattern, except for the first 25 Myr of lower mantle crossing and for the first part of upper mantle crossing, during which rather than the monotonically rising displacement, as in the case of phase-change interface, the chemical one is responsible for a small negative displacement or subsidence of the Earth's crust. This behavior is responsible for the generally lower values of the maximum displacements reached by chemical interfaces in comparison to phase-change ones.

[57] The trend of the curves for the cylinders, second row, after the top of the density anomaly hits the bottom of the lithosphere (thin vertical line) is different from the case of the column since the height of the cylinder is reduced until the bottom of the cylinder reaches the lithosphere-upper mantle interface at 36 Myr. When the bottom of the cylinder also reaches the bottom of the lithosphere, the anomaly totally disappears, leading to the vanishing of $\overline{U}(t, \overline{r}, \theta)$ after 35 Myr.

[58] Maximum displacements are generally lower for cylinders with respect to columns, especially for small radii. For example, for 100-km, thin solid curves, the displacement of 300 m for the column and phase-change interface, obtained from $\sim$3.0 ($100^2/10^2$) $\approx$ 300 m, is reduced to 130 m for the cylinder.

[59] Thinning of the elastic outer layer to 32.2 km, third and fourth rows, has the effect of increasing the maximum displacements, as visible from the almost factor 3 increase of the vertical scale in meters. A close inspection shows, on the other hand, that this increase of the displacements occurs, after crossing the 121 km depth, only for the smallest radii of the anomalies, columns or cylinders, which are, as expected, the most sensitive to the thickness of the elastic layer. If we compare in fact the largest radii of 600 km for the two lithospheric thicknesses, we note that displacements remains unchanged to 1 and 1.5 m for the unitary cross section, for both chemical and phase-change interfaces. This finding is also visible in the larger spreading between the solid and dashed curves for the 32.2-km-thick lithosphere once compared with the 121-km case. Decreasing the thickness of the elastic outermost layer has in fact the effect of reducing the ability of the latter to act as a low-pass filter, thus favoring the smallest loads which are the richest in high harmonic content.

[60] We could have considered plumes larger than 600 km in radius, but for the sake of clearness in Figure 6, we choose the most significant dimension (around 460 km) for comparison with the superplume of *Farnetani and Richards* [1994]. Furthermore, as we can notice in Figure 6, the trend of the function $\overline{U}(t, \overline{r}, \theta)$ for larger $\overline{r}$ can be easily extrapolated.

[61] From Figure 6, it is also possible to extrapolate the behavior of the Earth's surface for a plume starting from the upper-lower mantle interface. By fixing a new $t = 0$ in correspondence with the first gray line on the left, we have simply to shift the curves for the various radii in such a way that the new displacements are set to zero in correspondence to the new $t = 0$, thus deleting the contribution arising from the lower mantle, as easily obtainable from previous mathematical developments.

[62] Details of the plume are described by high degree components of the harmonic expansion and, as already shown, the portion of the Earth overlying the source acts as low-pass filter, meaning that the high harmonic degrees are severely cut, so that details in the structure of the source are not expected to be visible in the Earth's surface behavior. The effects of the filtering can be indirectly seen also in Figure 6, when the load is still in the mantle. In fact, Figure 6 shows the surface response due to sources of comparable masses, but of very different harmonic coefficients $L_\ell(r_s, \overline{r})$: in particular sources with large $\overline{r}$ have mainly low degree harmonic components, while those of small $\overline{r}$ have both low and high degree harmonic components. When the load is still deep in the mantle, from the curves of Figure 6, it is clear that for a wide range of $\overline{r}$ variation the curves are clustered: large variations in $\overline{r}$ correspond to a small variation in the function $\overline{U}(t, \overline{r}, \theta)$, which depends on $\overline{r}$ only through the harmonic coefficient $L_\ell(r_s, \overline{r})$ of the load.

[63] This means that filtering has severely reduced the difference between the various sources, by cutting the highest harmonic components. In particular, the deeper the source, the more effective the filtering of high frequencies, namely the reduction of the differences for varying $\overline{r}$. In other words, for a good qualitative analysis, the anomaly dimensions and its mass are the most effective factors to determine the Earth's surface behavior, while small-scale details, for example, the deviation from sfericity of the plume, are negligible, as long as the mass equivalence among the various sources is respected.

5.2. Earth's Elasticity

[64] In the previous section we have dealt with the effects of lithospheric thickness variations. Here we quantify the effects of elasticity of the entire Earth on surface swelling, in particular that of the mantle.

[65] We start by reminding that in general the radial displacement $U(t, \overline{r})$ can always be written as a sum of two separate contributions, an elastic and a viscous one,

$$U(t,\overline{r}) = U^E(t,\overline{r}) + U^V(t,\overline{r}), \tag{18}$$

where $\overline{r}$ is the radius of the load. To clarify this statement, consider the expression of radial displacement $U(t, \overline{r}, \theta)$ in equation (14) for a rising column, rearranged as follows:

$$U(t,\overline{r},\theta) = \frac{a}{M_T}\,\Delta\rho\, A_c \sum_\ell P_\ell(\cos\theta)\Big([h_\ell]^E(t,\overline{r}) + [h_\ell]^V(t,\overline{r})\Big), \tag{19}$$

where the transient part $[h_\ell]^T$ has been neglected and the fluid part $[h_\ell]^F$, entering equation (14), has been explicitly expressed in terms of the elastic and viscous contributions given in equations (12) and (13), modified to account for the disk coefficients $L_\ell(\overline{r})$ (equation (15)).

[66] We estimate the weight of the elastic term $U^E(t, \overline{r})$ with respect to the whole displacement $U(t, \overline{r})$. Instead of the ratio U^E/U, we define the estimator

$$R_{EV}(t) = \frac{\| U^E(t) \|}{\| U^E(t) \| + \| U^V(t) \|}. \tag{20}$$

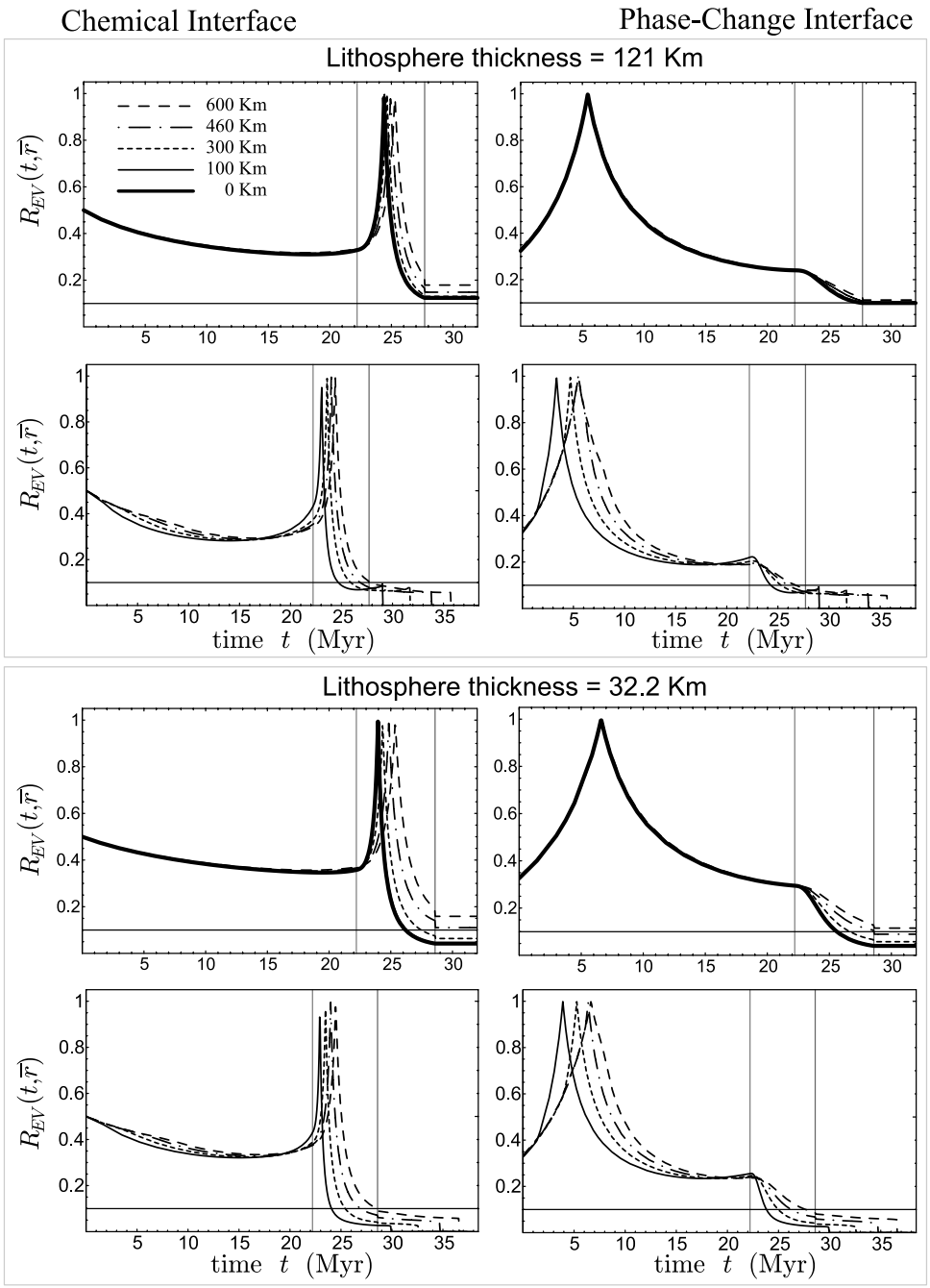

Figure 7. Using the same convention as Figure 6, R_{EV} plotted as a function of time from $t = 0$ Myr, when the density anomaly leaves the CMB, to $t = 32-37$ Myr.

[67] This definition avoids the singularity that would occur when U becomes zero. This would occur for $U^E = -U^V$, i.e., when both terms weight 50%: in this case $R_{EV} = 1/2$, thanks to the modulus functions at denominator. The definition of R_{EV} has the drawback of introducing spurious cusp structures due to the nondifferentiability of the modulus function.

[68] Following the same arrangement of Figure 6, namely a lithosphere of 121 km, two upper rows, and 32.2 km, two bottom rows, and first and third rows corresponding to columns and second and fourth ones to cylinders, Figure 7 shows the evolution in time of the ratio $R_{EV}(t, \bar{r})$, from $t = 0$, when the anomaly leaves the CMB, to 33 Myr, for different radii of the load; the two vertical grey lines indicate the time of the crossing of the upper-lower mantle boundary, left line, and the time of the arrival at the base of the lithosphere, right line. A model with a viscoelastic lithosphere of 32.2 km is presented in the same way in Figure 8. The cusp appearing in the whole set of panels, denoting an almost 100% elastic contribution, does not have a particularly important physical significance, simply indicating that the viscous contribution is almost zero, where the function R_{EV} is not differentiable.

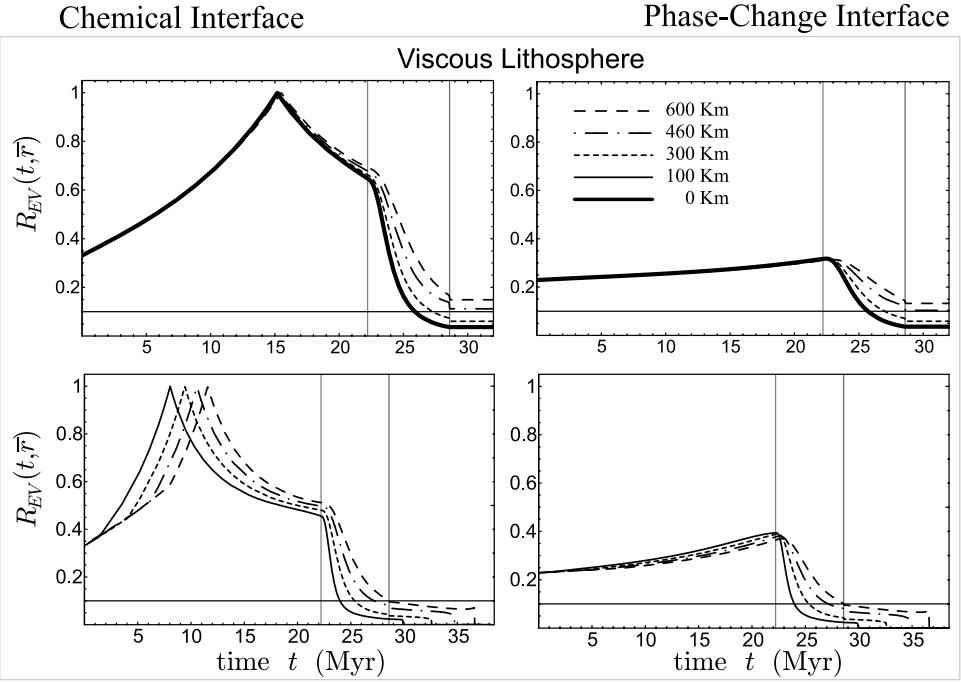

Figure 8. As for the two bottom rows of Figure 7, but for a viscous lithosphere of 32.2 km.

[69] Small viscous contributions generally occur when the density anomaly is close to a chemical boundary, so that the buoyant chemical interface dampens the viscous flow and the cusp is close to the upper-lower mantle interface. For phase-change interface, this occurs when the anomaly is close to the CMB, the only chemical boundary for this model.

[70] For phase-change interface, cusps are thus largely shifted to the left with respect to those for chemical interface. This is the main difference in the $R_{EV}(t)$ trend between the chemical and phase-change interface cases. Keeping in mind that the elastic contribution $U^E(t)$ is always positive, Figure 6 helps to understand this difference between chemical and phase-change interfaces in terms of the change in sign of the displacement $U(t)$, being negative for chemical interface in the lower mantle and part of the upper mantle as the leading viscous contribution. As the viscous term changes sign for chemical interface, approximatively at 25 Myr, the elastic contribution reaches its maximum. Change of sign of the $U(t)$ is barely visible for phase-change interface, 4 times smaller than 5 Myr.

[71] A noticeable feature of Figure 7 is that when the anomaly is located in the lower mantle the ratio R_{EV} is, for all cases, always above the 20% for phase-change interface and always above the 30% for chemical interface. Moreover, while the anomaly is rising through the upper mantle, $R_{EV}(t)$ decreases smoothly for the phase-change interface and more steeply for chemical cases after the cusp, until the anomaly reaches the lithosphere. After the head of the plume hits the bottom of the lithosphere, the total displacement $U(t)$ reaches its maximum (Figure 6), and the viscous contribution dominates over the elastic one; that is, the portion of the Earth overlying the source is too thin and its ability to dampen the viscous contribution is no more effective.

[72] The major role of elasticity when the anomaly is rising through the lower mantle is a consequence of the stiffness of the highly viscous 10^{22} Pa s lower mantle, while its role diminishes in the upper mantle which, being 30 times less viscous than the lower mantle, behaves like a fluid body. We can also notice that in general the trend of $R_{EV}(t)$ is qualitatively very similar in the two lithospheric models, comparing interfaces of identical nature.

[73] Variations in the $\bar{r}$ radius of the load, i.e., the dimensions of the load, have, in general, minor effects on $R_{EV}(t)$, without affecting the overall pattern of the curves. In fact, for rising columns through the lower mantle, the curves $R_{EV}(t, \bar{r})$ overlap, i.e., the ratio R_{EV} is essentially insensitive to the radius of the anomaly, for the considered range of radii.

[74] In general as already analyzed in previous sections, the dimension of the load becomes slightly more important while crossing the upper mantle. In a more detailed analysis, we can see that the effects of the reduction in the thickness of the elastic outer layer of the Earth from an average continental one (two first rows) to an average oceanic lithosphere (two bottom rows), is appreciable only at the end of the process, when the displacement $U(t)$ reaches its maximum, and mostly for the smallest anomalies. In fact, for larger anomalies (at least 460 km radius) the curves $R_{EV}(t, \bar{r})$ tend to remain at the same percentage, comparing the panels in the first and third rows. In general, for fixed load shape, columns or cylinders, the largest loads are thus the most effective in triggering the elastic behavior of the Earth.

[75] When the elastic lithosphere is replaced by an outermost viscoelastic layer, as the inner ones, the ratio $R_{EV}(t, \bar{r})$ behaves as shown in Figure 8. Although the viscous contribution is increased in the final stage when the head of the plume has reached the bottom of the lithosphere, an important elastic contribution still remains even for smallest loads, solid curves.

[76] The most noticeable difference with respect to Figure 7 is the disappearance of the cusps for the phase-

change interface cases, caused by the viscous contribution U^V increasing enough to keep R_{EV} always below 30%. For chemical interface cases, the cusp is shifted to the left; that is, in the upper mantle the increase of the viscous contribution U^V is enough to keep R_{EV} always below 70%.

[77] Figure 8 shows that even without the presence of a purely elastic lithosphere, the elastic contribution varies in the range of 10–30% of the total during the dynamic phase of the process when the anomaly crosses the upper mantle and persists at the bottom of the lithosphere for loads with moderate and large size radii of 460–600 km. The elastic contribution is reduced below 10% only for small size loads, of the order of 100 km.

[78] Elasticity enters to play a role in modeling rising plumes in a direct fashion through the thickness of the elastic outermost lithosphere but it enters also through the global elastic properties of the mantle, only slightly depending on the thickness of the lithosphere or on the shape or dimension of the load. Moreover it is clear that, from all cases of Figure 7 and 8, the correct description of rising masses through the mantle needs the elastic contribution. Also, even when the head hits the outermost layer, the surface displacement $U(t)$ is at its maximum and the ratio R_{EV} diminishes, the elastic contribution for medium and large size plumes is within 5 and 10%.

[79] The rheological nature and thickness of the outermost layer plays a crucial role in determining the percentage contribution of elasticity only in the very final stage when the surface swelling has reached its almost final height, while the global elastic properties of the planet plays a role, quantified by the percentages above, during the whole time evolution of the process. This result should not be surprising, since even in this typical mantle convection problem, thermal anomalies induce density anomalies as given by equation (8), which in turn trigger, independently from their amplitude, sizable elastic response as well as a viscous one, as expressed by equations (18) or (19).

[80] A step ahead in the physical understanding can be gained by coming back to Figure 4. Bearing in mind that we are dealing with Green functions evaluated at the surface of the Earth and that the elastic contribution is always lower than the viscous one, by comparing the first and the second rows of Figure 4, we note that the viscous component $[h_\ell]^V$ is more severely dampened with depth with respect to the elastic component $[h_\ell]^E$, which explains the general increase with depth in the mantle of R_{EV}.

6. Angular Dependence of the Radial Displacement

[81] Although the differences in the uplift behavior between models with chemical and phase-change interfaces, in view of the physical considerations presented in previous sections, only the model with phase-change interface will be considered from now on. Without claiming to simulate a real plume, the following three models are considered: (1) a column 300 km in radius, (2) a 300-km cylinder with an underling conduit 100 km in radius, and (3) a 460-km cylinder, in agreement with the general characteristics described in section 3.

[82] Figure 9 shows the radial displacement in kilometers as function of the distance, in kilometers, obtained from $\theta \times a$, where a is the radius of the Earth and θ denotes the angular distance from the anomaly, for a portion extending from $-\pi/10$ to $\pi/10$ with respect to the source. Under each surface displacement panel, a cartoon portrays the shape and position of the density anomaly, from the Earth's surface to the CMB. As indicated by the cartoons, the first row corresponds to 22.2 Myr, when the head of the anomaly hits the upper-lower mantle interface, the second one to 27.7 Myr, when the head hits the bottom of the 121 km lithosphere and the third one to 28.6 Myr, when the head hits the bottom of the 32.2 km lithosphere. Solid and dashed curves correspond to lithospheric thickness of 121 and 32.2 km.

[83] Independently from the shape of the anomaly, the plume crossing the whole lower mantle produces a swelling of the order of hundred meters: the swelling of kilometers, as shown in the second and third row, is built mainly during the ascent of the plume head in the upper mantle. The second and third rows show that in the time interval of 0.9 Myr, during which the plume head crosses the portion of the upper mantle from the depth of 121 km to the bottom of the thin lithosphere, the swelling for the thick lithosphere case, solid line, stops growing, since the head already reached the bottom of the elastic layer, while the one for the thin lithosphere continues to grow, from the 2–3 km of the second row to about 4 km of the third row, shedding light on the importance of the crossing of the uppermost upper mantle for the thin lithosphere case.

[84] From top to bottom, the swelling for the thin lithosphere of 32.2 km becomes progressively larger with respect to the 121 km case, as the plume head gets closer to the Earth's surface. Thinning of the lithosphere has thus a major effect on the amplitude of the swelling in the final stage, the thin with respect to the thick lithosphere doubling the height of the "bell" curve, as shown in the third row. From the lower to the upper mantle, the lateral extension of the "bell" curves is subject to reduction.

[85] Although the shape and height of the "bell" curves are quite similar to those of *Farnetani and Richards* [1994] (their Figure 8, the fourth graph), when the 460-km plume and the lithosphere of 32.2 km are considered, their curve seems to reach negative value around 600 km while ours becomes negative only after 2000 km (Figure 10): This difference can be explained by the flexural properties of the elastic lithosphere in the present normal mode modeling. In this perspective, it is remarkable that, from 22.2 to 27.7 or 28.6 Myr, the uplift grows in the central part of the bell, while its flanks remain unaffected during the time interval from 21 to 28 Myr, as shown by the stability of the radial displacement at 1000 km from the center. The details of the deformation in the periphery with respect to the central, notably uplifting region will be considered in Figure 10.

[86] By comparing the various plume models, we note the reduction in the amplitude of the displacement, from the first to the second columns, due to the reduction of the plume head in spite of the presence of the thin conduit. The flexural response of the lithosphere to the rising cylinder is thus qualitatively different from the cases characterized by a persistent density anomaly beneath the plume head.

[87] Figure 10 deals with the small amplitude displacements of the order of tens of meters in the periphery with

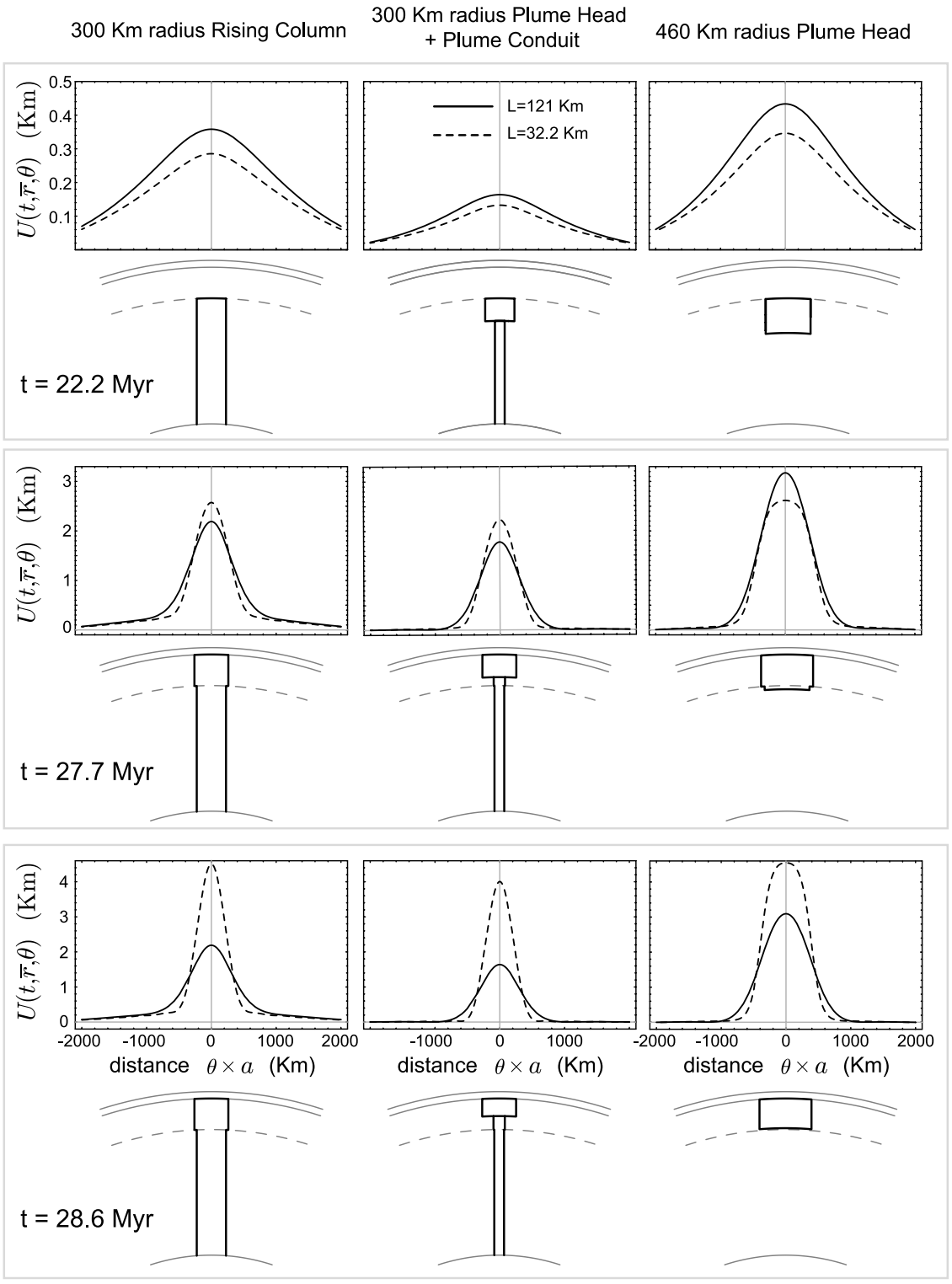

Figure 9. Surface deformation $U(t, \bar{r}, \theta)$ for (left) a rising column, (middle) a plume plus conduit, and (right) plume head, as a function of θ, in terms of $\theta \times a$ where a denotes the Earth radius and θ is in radians. The interval ranges from 0 to $\pi/10$. First, second, and third rows correspond to 22.2, 27.7, and 28.6 Myr. Cartoons portray the corresponding plume configuration.

respect to the large upwarping of the crust over the rising density anomaly, with the horizontal axis reaching the distance of about 20,000 km at 180° from the anomaly. Solid and dashed curves stand for the 121- and 32.2-km-thick lithosphere, while the gray curve portrays the purely elastic contribution, for the 32.2-km lithosphere. From the top to the bottom panels, the three cases of Figure 9 are considered, the first and second columns corresponding to

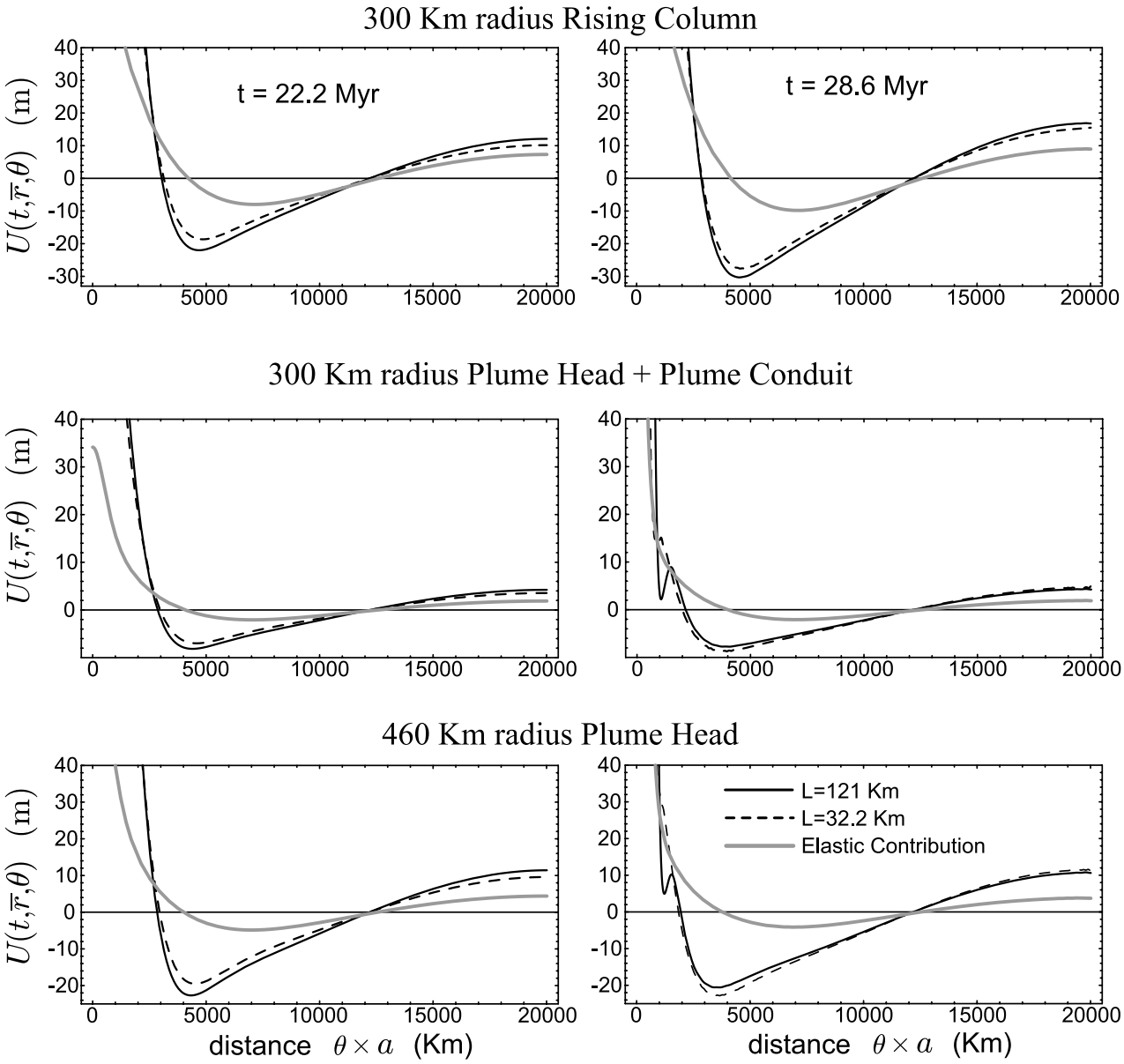

Figure 10. Surface deformation $U(t, \bar{r}, \theta)$ as a function of the distance in kilometers from the center of the swelling, where the distance is given by terms of $\theta \times a$, where a denotes the Earth radius and θ is in radians, from 0 to π. The vertical scale is chosen in such a way to enlighten the far field displacements of at most tens of meters. The central swell is out of scale. Displacements are evaluated for (left) 22.2 Myr and (right) 28.6 Myr. First, second, and third rows stand for a 300-km rising column, a 300-km plume head plus conduit, and a 460-km plume head. Solid, dashed, and gray curves stand for a 121-km-thick elastic lithosphere, a 32.2-km-thick elastic one, and for the purely elastic contribution, for the 32.2-km lithosphere.

22.2 and 28.6 Myr, as for the first and third row of Figure 9, when the plume head hits the upper-lower mantle interface and the bottom of the 32.2-km-thick lithosphere. The major feature of this figure is the broad region of negative displacement, or subsidence, of the Earth's entire lithosphere. This subsidence, while reaching a minimum varying between about -10 to -30 m, is distributed from about 3000 to 13,000 km from the crust's maximum upwarping. A smaller amplitude upwarping of the lithosphere that is due to the flexural reaction to such global subsidence appears from a distance of about 13,000 km to the antipodes with respect to the rising plume.

[88] Deviations between thick and thin elastic lithospheres are minor in the far field. It is noteworthy that elastic contribution is important in the far field in terms of relative amplitude with respect to the total displacement and that it is smoother than the total displacement, as expected, since elasticity prevents too large a bending of the plates. These global features, as will be shown afterward, impact sea level changes induced by plumes. This finding, related to the global response of the lithosphere to rising plumes, is qualitatively different from that obtained by *Farnetani and Richards* [1994] and *Griffiths and Campbell* [1991], where the limited lateral extension of the boxes where the numer-

ical and analogical experiments are carried out impedes simulation of the sphere's global response.

7. Sea Level Changes Induced by Plumes

[89] The sea level $SL(t, \theta, \varphi)$ is defined by *Mitrovica and Milne* [2003] as the difference between the equipotential surface represented by the geoid $G(t, \theta, \varphi)$ and the solid surface of the Earth $R(t, \theta, \varphi)$. It is defined over the whole surface of the Earth, including the dry lands, although sea level can be projected and appropriately defined over the oceans by means of the ocean function $C(t, \theta, \varphi)$, defined as to take the unitary value over the oceans and zero over the lands [*Munk and MacDonald*, 1960].

[90] Changes in $\Delta SL(t, \theta, \varphi)$ are governed by several factors like surface deformation due to the main driver, as with internal loads considered here, and the associated redistribution of the ocean water and can be described in terms of the formalism introduced by *Farrel and Clark* [1976] and reworked by *Mitrovica and Milne* [2003]; for surface load such as ice loading, *Mitrovica and Milne* [2003], in their equation (I1) provide the following expression for the changes $\Delta SL(t, \theta, \varphi)$:

$$\Delta SL(t,\theta,\varphi) = \frac{\rho_I}{g}\Phi_I * I + \frac{\rho_W}{g}\Phi_O * \Delta SL + C_{SL}(t), \qquad (21)$$

where ρ_I and ρ_W denote the densities of the ice and water, g the gravity at the surface, θ and φ are the latitude and the longitude and t is time. I describes the evolution in time and space of the ice load. The function Φ is defined as

$$\Phi = \phi' - Ug, \qquad (22)$$

where ϕ' and U denote the Green functions whose harmonic coefficients are defined in equation (3). The asterisk $*$ denotes convolution in space and time, while the subscripts I e O indicate that convolution is limited to the geometries of the ice load and oceans, respectively. The term $C_{SL}(t)$ entering equation (I1) of *Mitrovica and Milne* [2003] is given by

$$C_{SL}(t) = -\frac{M_I(t)}{A_O\,\rho_W} - \frac{1}{A_O}\left\langle \frac{\rho_I}{g}\Phi_I * I + \frac{\rho_W}{g}\Phi_O^* \Delta SL \right\rangle_O, \qquad (23)$$

where the brackets $\langle\rangle_O$ indicate integration over the surface of the oceans. The first term on the right of equation (23) is named eustatic sea level change by *Mitrovica and Milne* [2003], while the second term can be defined as a spatially uniform shift in the sea-surface necessary to conserve mass of the oceans when taking into account all gravity and crustal variations (J. X. Mitrovica, personal communication, 2005). It should be borne in mind that this definition of eustasy does not include changes in the volume of ocean basins, as done by *Hardebeck and Anderson* [1996], where in their Figure 1 they include swells, plateaus and ridges as sources of eustatic sea level changes. In order to avoid confusion in the various definitions of eustatic sea level changes, and to compare our results with sea level changes due to tectonics, we will consider the integral over the oceans entering equation (23) as comparable with changes due to tectonic processes, as done by *Hardebeck and Anderson* [1996], widening the significance of eustasy limited to water exchange between ice masses and oceans, as done in post-glacial rebound studies.

[91] Equation (21) for sea level changes is an integral equation since the unknown $\Delta SL(t, \theta, \varphi)$ appears both in the right and left members of the equation, for whose solution *Mitrovica and Peltier* [1991] first implemented a new spectral formalism. Once equations (21) and (23) are properly modified, they can be used to evaluate sea level changes due to internal loads, which induce only surface deformation without adding or extracting water from the oceans. The function I and the density ρ_I in equations (21) and (23) is thus changed into the appropriate loading function L for internal loads and $C_{SL}(t)$ is defined without the term containing the melting ice. The sea level equation can be simplified, though remaining a useful tool to estimate both local sea level changes, via $\Delta SL(t, \theta, \varphi)$ and global variations, via $C_{SL}(t)$, by neglecting the indirect effects of water redistribution over the oceans, which is appropriate if the dominant mechanism driving these changes is the direct effect of the internal load. Thus sea level equation (21) becomes

$$\Delta SL(t,\theta,\varphi) = \frac{1}{g}\Phi * L + C_{SL}(t), \qquad (24)$$

where

$$C_{SL}(t) = -\frac{1}{A_O}\langle \frac{1}{g}\Phi * L\rangle_O, \qquad (25)$$

which is actually a global sea level change.

[92] Notice that equation (24) is no longer an integral equation. If we consider the relative sea level changes

$$RSL = \phi'/g - U \qquad (26)$$

defined as by *Piromallo et al.* [1997], then, by using the definition of Φ (equation (22)), $C_{SL}(t)$ is given by the spatial integral over the ocean of the function $RSL(t, \theta, \varphi)$ (i.e., the convolution of RSL with the load function L) divided by the ocean area. Unlike ΔSL, RSL does not contain the term $C_{SL}(t)$.

8. Global Sea Level Changes Induced by the Mid-Cretaceous Superplume

[93] Global sea level changes, as shown in the previous section, depends on the distribution of the oceans or, equivalently, of dry lands. For plumes, the most interesting case to study is surely the superplume event purported to have occurred during the mid-Cretaceous [*Larson*, 1991a], when land and ocean distribution was different from present day's.

[94] Before facing the evaluation of the global sea level changes modeled on the mid-Cretaceous superplume, let us consider the relative sea level changes RSL, defined as in equation (26), owing to the three plume models of previous sections. In Figure 11, for each plume model, the top, middle and bottom rows show the radial displacement of the Earth's surface $U(t)$, the geoid displacement $\phi'(t)/g$ and RSL as evaluated over the upwelling density anomaly so as to capture the maximum signal as a function of time; solid curves correspond to the 121-km-thick lithosphere and the

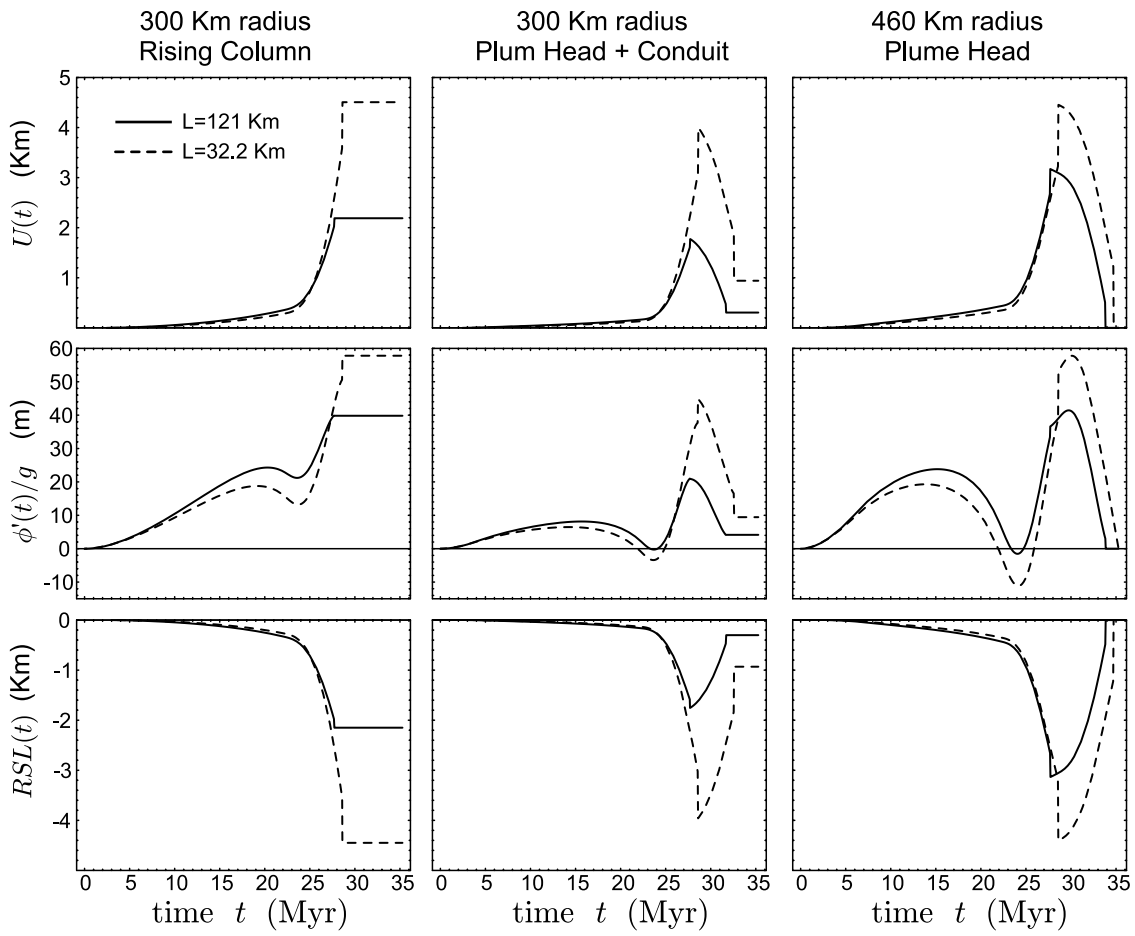

Figure 11. (top) Radial displacement $U(t)$, (middle) geopotential $\phi'(t)/g$, and (bottom) relative sea level *RSL*. From the left to the right column, the three plume models are considered, as indicated by the headings. Time is in Myr from the initiation of the process, when the density anomaly leaves the CMB. The fields are evaluated at the Earth surface on the top of the anomaly. Solid and dashed curves stand for a lithosphere of 121 and 32.2 km of thickness, respectively.

dashed ones to the 32.2-km-thick one. The radial displacement is about 2 orders of magnitude larger than the geoid shift, implying, from the definition of *RSL*, that changes in relative sea level are mainly controlled by the displacement of the sea-bottom. The values of U, ϕ'/g and *RSL* when the head plume hits the bottom of the lithosphere are mainly controlled by the thickness of the elastic outer layer, reaching their maximum for the thin lithospheric model, dashed curves versus solid ones. Thinning of the lithosphere has, in fact, the effect of doubling U and *RSL* at least for the rising column and plume head plus conduit, first two columns. Over the anomaly, relative sea level fall is of the order of kilometers.

[95] It was on the basis of the volume of the large upwarping or superswell of the Earth's crust, resulting from the plume head, obtained by other kinds of plume modeling which provided similar results to those in Figure 9 in terms of swelling, that *Hardebeck and Anderson* [1996] suggested that the mid-Cretaceous superplume event should have produced a sea level rise, that they propose to be added to the list of sea level changes responsible for eustasy, ranging between 100 and 220 m, as shown in their Figure 1, thus conflicting with sea level rise due to oceanic crust production. It is generally accepted that in the time interval between 125–120 and 90 Myr before the present, the superplume related to the Ontong Java Plateau rose up to the bottom of the lithosphere, with dry lands considerably drifting apart in that time interval.

[96] A rough estimate can be given on the basis of few considerations. First, the land masses at the beginning of the mid-Cretaceous were still patched together within the Gondwana supercontinent. As a first approximation, it is possible to model the Gondwana supercontinent by means of a spherical cap covering one fourth of the Earth's surface located at the antipodes of the superswell. The second approximation is to assume that during the whole time evolution of the process from the beginning of the plume formation at the CMB until it reaches the lithosphere, land distribution remains unchanged. The global sea level change $C_{SL}(t)$, for the cap-shaped continent, namely the integral of *RSL* over the oceans, in terms of harmonic coefficients becomes

$$[C_{SL}]_\ell(t) = \frac{2\pi a^2}{A_{Oc}} \left(\int_0^{\frac{2}{3}\pi} P_\ell(\cos\theta) \sin\theta \, d\theta \right) \left(\frac{\phi'_\ell(t)}{g} - U_\ell(t) \right), \tag{27}$$

where $A_{Oc} = \frac{3}{4} A_{Sphere}$ or $A_{Oc} = 3\pi a^2$.

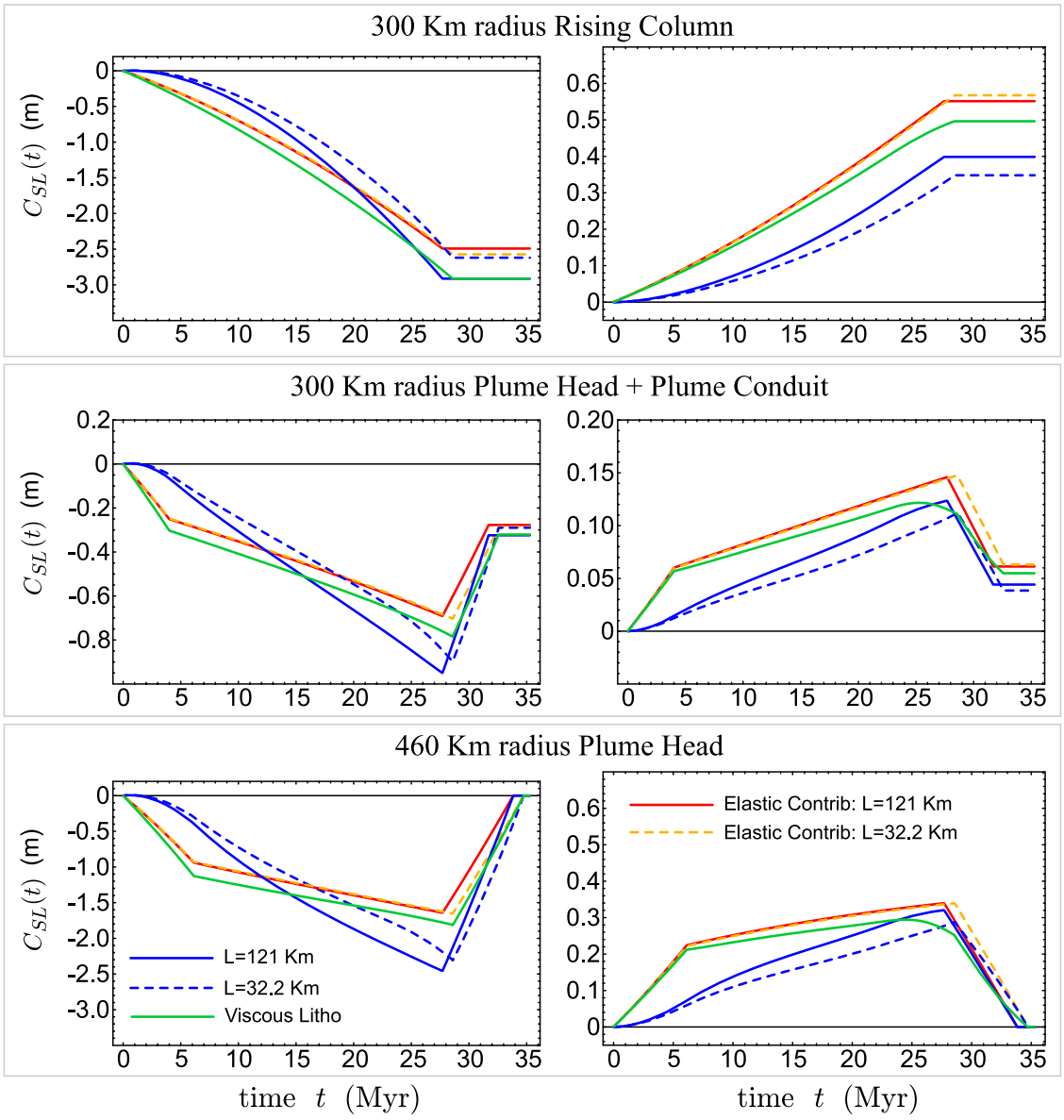

Figure 12. $C_{SL}(t)$ for (left) the simplified cap-shaped Gondwana supercontinent and (right) realistic dry land distribution, as a function of time. First, second, and third rows stand for a 300-km rising column, a 300-km plume head plus conduit, and a 460-km plume head. Meaning of the curves is given in the insets.

[97] If $O_\ell = \int_0^{\frac{2}{3}\pi} P_\ell(\cos\theta)\sin\theta\, d\theta$ denotes the ocean function coefficients for this simple cap-shaped land distribution, the global sea level change becomes

$$C_{SL}(t) = -\frac{2}{3}\sum_\ell O_\ell\left(\frac{\phi'_\ell(t)}{g} - U_\ell(t)\right). \tag{28}$$

A more realistic dry land-distribution, which yet remains unchanged during the plume rise, can be considered. Thus, instead of the O_ℓ coefficients, those for a more realistic distribution can be employed via integration, such as that corresponding to 90 Myr ago when the plume head hits the lithosphere and the latter's response is the largest in terms of *RSL* and thus in terms of C_{SL}.

[98] Figure 12 shows the results for $C_{SL}(t)$ for both cap-shaped supercontinent, left column, and for realistic land distribution, right column. First, second and third rows stand for the three plume models, as noted on the top of each row. Blue curves, solid and dashed, stand for the lithospheric thickness of 121 and 32.2 km, and the green curve corresponds to the viscoelastic lithosphere of 32.2 km. The red and orange curves correspond to cases where only the elastic part is considered, with solid (red) and dashed (orange) ones standing for lithospheric thickness of 121 and 32.2 km; notice that the orange curves is the elastic contribution also for the model with viscoelastic lithosphere.

[99] Independently from varying thickness and rheology of the lithosphere, or even limiting the contribution to $C_{SL}(t)$ to the elastic one, the pattern of $C_{SL}(t)$ remains substantially stable, both in shape and amplitude, except for the knees for plume heads, due to subtraction of a column to simulate cylinders, as shown in equation (17). The amplitude of $C_{SL}(t)$ is at most of a few meters, the largest value of about 3 m for the

cap-shaped supercontinent while of few tens of centimeters for realistic land distribution. It is reasonable to assume that the most realistic case stands between the two end-member simulations. Note that global sea level sign is opposite for the two land distributions, the cap shaped producing a global sea level fall and the more realistic one a small global sea level rise, and that these results do not depend on the plume model, except for the fact that $C_{SL}(t)$ amplitude is subject to reduction after the plume head hits the bottom of the lithosphere since the density anomaly slowly disappears afterward.

[100] Comparison between blue and orange dashed curves, and close resemblance of the green curve for the viscoelastic outer layer with orange ones, shows that global contribution to global sea level changes due to $C_{SL}(t)$ are mainly elastically supported, elasticity never contributing less than 30% to the highest signal, in complete agreement with findings of Figures 7 and 8. Besides the fact that the global quantity such as the "eustatic" sea level is mainly elastically supported, two important conclusions can thus be drawn from these results: $C_{SL}(t)$ is not of the order of 10^2 m as suggested by *Hardebeck and Anderson* [1996] and the amplitude, as well as the sign of global sea level changes, are very sensitive to land distribution.

[101] Findings on relative sea level *RSL* changes can be better exploited in Figure 13 over the entire Earth, with the superplume placed in the Pacific and land distribution is from paleomaps of 90 Myr ago, in agreement with the paleoreconstruction given by *Coffin et al.* [1998], for the three plume models. Since the scale is of the order of tens of meters, the large relative sea level *RSL* falls over the plume are out of scale. Independently from the plume model, column, cylinder-plus-conduit and cylinder, top to bottom, these figures show a wide region of relative sea level rise, corresponding to the global subsidence surrounding the swelling enlightened in Figure 10, extending outward from the concentrated superswell in the Pacific for thousands of kilometers. The amplitude of relative sea level rise is smaller in amplitude than the relative sea level fall over the superswell but extends over a large area in comparison to the concentrated swell over the upwelling plume. Owing to the plume, the Earth becomes elongated along an axis passing through the density anomaly and is thus squeezed along a circular belt perpendicular to this axis.

[102] Concentrated relative sea level fall and diffused relative sea level rise offset each other, in agreement with mass-conservation principle, thus causing changes in $C_{SL}(t)$ obtained from the integration over the oceans of *RSL* portrayed in Figure 13 of at most a few meters, as shown in Figure 12, much smaller than the mid-Cretaceous eustatic change of the order of 10^2 m. The global subsidence stores the water displaced by the superswell, thus counteracting the effects of the plume on global "eustatic" sea level rise.

9. Conclusions

[103] The upwelling of a plume has been modeled by means of normal mode theory in viscoelasticity. The presence of the elastic lithosphere accounts for the planet's flexural response to the plume, even at considerable distances from the upwelling.

[104] Convective models can efficiently simulate the plume and its kinematics, but the global deformation induced by upwelling can be better dealt with by the normal mode approach in viscoelasticity, which makes the two schemes complementary. The consistency of the topography over the upwelling material with that obtained within the framework of totally different models, based on mantle convection driven by temperature and density contrasts, proves the robustness of our approach, once plume kinematics is based on the results of convective models.

[105] Furthermore, this consistency is another demonstration of the marginal role played by details of the shape of the plume. This justifies the use of cylinders rather than spheres, even if the latter are of common use in these kind of simulations. Moreover, besides the absence of a consolidated plume model and in view of the highly debated shape and other features of the plume in terms of both modeling and seismic imaging, the present study with the use of a cylinder considered as an elementary mass anomaly, provides a powerful instrument for future studies on more realistic mantle structures.

[106] For internal loads, the normal mode solution requires summation only up to harmonic degree $\ell = 100$, mainly because the outermost portion of the planet acts as a low-pass filter. Furthermore, the very long times of upwelling and the large plume dimensions make it possible to neglect the transient part of the solution and to treat solely the steady state part (fluid limit); for point-like sources, on the contrary, the transient part is important, as *Ricard and Sabadini* [1990] have shown.

[107] Although the most prominent feature of the swell or superswell, i.e., its amplitude, agrees with convective models, normal mode modeling differs from convective ones in terms of such global features as the wide depression surrounding the swell for thousands of kilometers, thereby playing a crucial role in the interpretation of the global effects of the swell, such as global sea level changes. Once the planet's global flexural properties are taken into account, as in the present analysis, the global subsidence around the swell counteracts the sea level rise caused by the swelling of the lithosphere, leading to a C_{SL} that is accumulated over the whole time history of the plume and ranging from a few centimeters to at most a few meters, with the sign dependent on real continent distribution. Given these findings, "eustatic" sea level rise of about 100–220 m as proposed by *Hardebeck and Anderson* [1996], as being due to the swell of the lithosphere over the impinging plume, has to be revised, since their estimate is based solely on the volume of the swell emplaced on the top of the oceanic crust and does not account for the global subsidence surrounding the swell itself. The eustatic sea level data for the mid-Cretaceous can thus not be used to reject the hypothesis of the simultaneous occurrence of large oceanic crust production and of a superplume [*Larson*, 1991a, 1991b].

Figure 13. Relative sea level *RSL* as a function of θ e φ over the globe, for the three plume models, as indicated on the top of each panel, evaluated at the time in which the head of the anomaly hits the bottom of the lithosphere. The dry land distribution corresponds to 90 Myr ago, and the plume is positioned in the Pacific Ocean beneath the Ontong Java Plateau, in agreement with the paleoreconstruction given by *Coffin et al.* [1998].

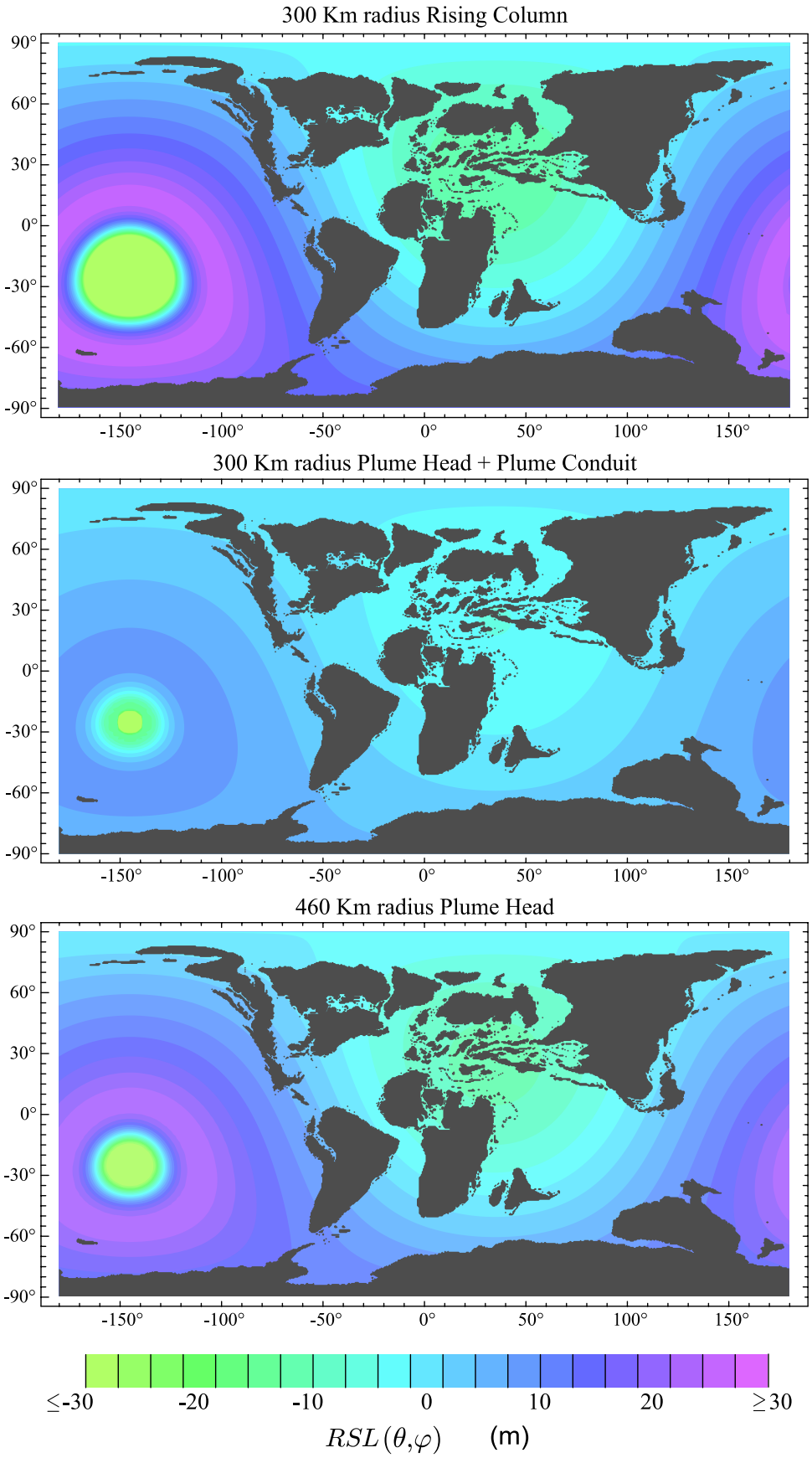
300 Km radius Rising Column
300 Km radius Plume Head + Plume Conduit
460 Km radius Plume Head
90°
60°
30°
0°
-30°
-60°
-90°
-150°
-100°
-50°
0°
50°
100°
150°
≤-30
-20
-10
0
10
20
≥30
RSL(θ,φ) (m)

Figure 13

[108] By going further with respect to the analysis by *Ricard and Sabadini* [1990] where attention was drawn on transient effects of viscoelastic coupling for mantle density anomalies, we show that elasticity plays a non negligible role in typical mantle convection problems such as mantle plumes. Our findings provide indications that it is highly meaningful to make efforts toward a self-consistent approach for viscoelastic convection, as presented by *Muhlhaus and Regenauer-Lieb* [2005]. The Earth is simultaneously elastic and viscous, where viscous properties impact short-timescale processes of the order of 10^3 years as in Post-Glacial Rebound and, at the same time, elasticity impacts long-timescale processes, such as TPW, of 10^8 years, or, as considered here, plume upwelling of 10^7 years.

[109] **Acknowledgments.** We are indebted to the Associate Editor, Alessandro Forte, and an anonymous reviewer for their thorough review of the manuscript and for their important suggestions. This work is supported by the M.I.U.R. 2004 PRIN grant. We thank Elisabetta Erba for important suggestions and David Verzoni for continual help.

References

Coffin, M. F., and O. Eldholm (1993), Scratching the surface: Estimating dimensions of large igneous provinces, *Geology*, *21*, 515–518, doi:10.1130/0091-7613 (1993)]021<0515:STSEDO>2.3.CO;2.

Coffin, M. F., L. A. Lawver, and L. Gahagan (1998), Atlas of paleogeographic reconstruction, *Tech. Rep. 181*, 88 pp., Inst. of Geophys., Univ. of Texas at Austin, Austin.

Dalla Via, G., R. Sabadini, G. De Natale, and F. Pingue (2005), Lithospheric rheology in southern Italy inferred from postseismic viscoelastic relaxation following the 1980 Irpinia earthquake, *J. Geophys. Res.*, *110*, B06311, doi:10.1029/2004JB003539.

Dobrestov, N. L., A. G. Kirdyashkin, and A. A. Kirdyashkin (2003), Physicochemical condition at the core-mantle boundary and formation of thermochemical plumes, *Dokl. Acad. Sci. USSR, Earth Sci. Ser., Engl. Transl.*, *393A*, 1319–1322.

Dziewonski, A. M., and D. L. Anderson (1981), Preliminary reference Earth model, *Phys. Earth Planet Inter.*, *25*, 297–356, doi:10.1016/0031-9201 (81)90046-7.

Farnetani, C. G., and M. A. Richards (1994), Numerical investigation of the mantle plume initiation model for flood basalt events, *J. Geophys. Res.*, *99*, 13,813–13,833.

Farrel, W. E. (1972), Deformation of the Earth by surface loads, *Rev. Geophys.*, *10*, 761–797.

Farrel, W. E., and J. A. Clark (1976), On postglacial sea level, *Geophys. J. R. Astron. Soc.*, *46*, 647–667.

Forte, A. M., and R. L. Woodward (1997), Seismic-geodynamics constraints on three-dimensional structure, vertical flow, and heat transfer in the mantle, *J. Geophys. Res.*, *102*, 17,981–17,994.

Greff-Lefftz, M. (2004), Upwelling plumes, superswells and true polar wander, *Geophys. J. Int.*, *159*, 1125–1137, doi:10.1111/j.1365-246X.2004.02440.x.

Griffiths, R. W., and I. H. Campbell (1990), Stirring and structure in mantle starting plumes, *Earth Planet Sci. Lett.*, *99*, 66–78, doi:10.1016/0012-821X (90)90071-5.

Griffiths, R. W., and I. H. Campbell (1991), Interaction of mantle plume heads with the Earth's surface and onset of small-scale convection, *J. Geophys. Res.*, *96*, 18,295–18,310.

Gurnis, M., J. X. Mitrovica, J. Ritsema, and H.-J. Van Heijst (2000), Constraining mantle density structure using geological evidence of surface uplift rates: The case of the African Superplume, *Geochem. Geophys. Geosyst.*, *1*(7), doi:10.1029/1999GC000035.

Hardebeck, J., and D. L. Anderson (1996), Eustasy as a test of Cretaceous superplume hypothesis, *Earth Planet Sci. Lett.*, *137*, 101–108, doi:10.1016/0012-821X (95)00222-X.

James, T. S., and E. R. Ivins (1997), Global geodetic signatures of the Antarctic ice sheet, *J. Geophys. Res.*, *102*, 605–633.

Kirdyashkin, A. G., I. N. Gladkov, and V. N. Sharapov (1987), Modeling the dynamics of magma formation above local sources of heat (in Russian), *Geol. Geophys.*, *11*, 89–123.

Kumagai, I. (2002), On the anatomy of mantle plumes: Effect of the viscosity ratio on entrainment and stirring, *Earth Planet Sci. Lett.*, *198*, 211–224, doi:10.1016/S0012-821X (02)00513-7.

Larson, L. R. (1991a), Latest pulse of Earth: Evidence for a mid-Cretaceous superplume, *Geology*, *19*, 547–550, doi:10.1130/0091-7613 (1991)019<0547:LPOEEF>2.3.CO;2.

Larson, L. R. (1991b), Geological consequences of superplumes, *Geology*, *19*, 963–966, doi:10.1130/0091-7613 (1991)019<0963:GCOS>2.3.CO;2.

Le Meur, E., and R. C. A. Hindmarsh (2000), A comparison of tow spectral approaches for computing the Earth response to surface loads, *Geophys. J. Int.*, *141*, 282–298, doi:10.1046/j.1365-246x.2000.00068.x.

Lithgow-Bertelloni, C., and P. Silver (1998), Dynamic topography, plate driving forces, and African superswell, *Nature*, *395*, 269–272, doi:10.1038/26212.

Marquart, G., H. Schmeling, G. Ito, and B. Schott (2000), Condition for plumes to penetrate the mantle phase boundaries, *J. Geophys. Res.*, *105*, 5679–5693, doi:10.1029/1999JB900413.

Mitrovica, J. X., and A. M. Forte (2004), A new inference of mantle viscosity based upon joint inversion of convection and glacial isostatic adjustment data, *Earth Planet. Sci. Lett.*, *225*, 177–189, doi:10.1016/j.epsl.2004.06.005.

Mitrovica, J. X., and G. A. Milne (2003), On post-glacial sea level: I. General theory, *Geophys. J. Int.*, *154*, 253–267, doi:10.1046/j.1365-246X.2003.01942.x.

Mitrovica, J. X., and W. R. Peltier (1989), Pleistocene deglaciation and the global gravity field, *J. Geophys. Res.*, *94*, 13,651–13,671.

Mitrovica, J. X., and W. R. Peltier (1991), On postglacial geoid subsidence over the equatorial oceans, *J. Geophys. Res.*, *96*, 20,053–20,071.

Montelli, R., G. Nolet, F. A. Dahlen, G. Masters, E. R. Engdahl, and S. H. Hung (2004), Finite-frequency tomography reveals a variety of plumes in the mantle, *Science*, *303*, 338–343, doi:10.1126/science.1092485.

Morgan, W. J. (1971), Convection plumes in the lower mantle, *Nature*, *230*, 42–43, doi:10.1038/230042a0.

Morgan, W. J. (1972), Plate motion and deep mantle convection, *Mem. Geol. Soc. Am.*, *132*, 7–22.

Muhlhaus, H.-B., and K. Regenauer-Lieb (2005), Towards a self-consistent plate mantle model that includes elasticity: Simple benchmarks and application to basic modes of convection, *Geophys. J. Int.*, *163*, 788–800, doi:10.1111/j.1365-246X.2005.02742.x.

Munk, W. H., and G. J. F. MacDonald (1960), *The Rotation of the Earth*, Cambridge Univ. Press, New York.

Peltier, W. R. (1974), The impulse response of a Maxwell Earth, *Rev. Geophys.*, *12*, 649–669.

Phinney, R. A., and R. Burridge (1973), Representation of the elastic-gravitational excitation of a spherical Earth model by generalized spherical harmonics, *Geophys. J .R. Astron. Soc.*, *34*, 451–487.

Piromallo, C., G. Spada, R. Sabadini, and Y. Ricard (1997), Sea-level fluctuations due to subduction: The role of mantle rheology, *Geophys. Res. Lett.*, *24*, 1587–1590, doi:10.1029/97GL01561.

Ricard, Y., and R. Sabadini (1990), Rotational instabilities of the Earth induced by mantle density anomalies, *Geophys. Res. Lett.*, *17*, 627–630.

Richards, M. A., and B. H. Hager (1984), Geoid anomalies in a dynamic Earth, *J. Geophys. Res.*, *89*, 5987–6002.

Richards, M. A., R. A. Duncan, and V. E. Courtillot (1989), Flood basalts and hot-spot tracks: Plume heads and tails, *Science*, *246*, 103–107.

Riva, R. E. M., and L. L. A. Vermeersen (2002), Approximation method for high degree harmonics in normal mode modeling, *Geophys. J. Int.*, *151*, 309–313, doi:10.1046/j.1365-246X.2002.01754.x.

Sabadini, R., and L. L. A. Vermeersen (2004), *Global Dynamics of the Earth: Application of Normal Mode Relaxation Theory to Solid-Earth Geophysics*, *Mod. Approaches Geophys.*, vol. 30, Springer, New York.

Sabadini, R., D. A. Yuen, and E. Boschi (1982), Polar wander and the forced responses of a rotating, multilayered, viscoelastic planet, *J. Geophys. Res.*, *87*, 2885–2903.

Sabadini, R., C. Doglioni, and D. A. Yuen (1990), Eustatic sea-level fluctuations induced by polar wander, *Nature*, *345*, 708–709, doi:10.1038/345708a0.

Sabadini, R., A. M. Marotta, R. De Franco, and L. L. A. Vermeersen (2002), Style of density stratification in the mantle and true polar wander induced by ice loading, *J. Geophys. Res.*, *107*(B10), 2258, doi:10.1029/2001JB000889.

Schilling, J.-G. (1991), Fluxes and excess temperatures of mantle plumes inferred from their interaction with migrating mid-ocean ridges, *Nature*, *352*, 397–403, doi:10.1038/352397a0.

Spada, G., D. A. Yuen, R. Sabadini, P. J. Morin, and P. Gasperini (1990), A computer-aided, algebraic approach to the post-glacial rebound problem, *Math. J.*, *1*, 65–69.

Spada, G., Y. Ricard, and R. Sabadini (1992a), Excitation of true polar wander by subduction, *Nature*, *360*, 452–454, doi:10.1038/360452a0.

Spada, G., R. Sabadini, D. A. Yuen, and Y. Ricard (1992b), Effects on post-glacial rebound from the hard rheology in the transition zone, *Geophys. J. Int.*, *109*, 683–700.

Tosi, N., R. Sabadini, A. M. Marotta, and L. L. A. Vermeersen (2005), Simultaneous inversion for the Earth's mantle viscosity and ice mass imbalance in Antarctica and Greenland, *J. Geophys. Res.*, *110*, B07402, doi:10.1029/2004JB003236.

Van Keken, P. (1997), Evolution of starting mantle plumes: A comparison between numerical and laboratory models, *Earth Planet Sci. Lett.*, *148*, 1–11, doi:10.1016/S0012-821X (97)00042-3.

Watson, S., and D. McKenzie (1991), Melt generation by plumes: A study of Hawaiian volcanism, *J. Petrol.*, *12*, 501–537.

Watts, A. B. (1978), An analysis of isostasy in the world's oceans: 1. Hawaiian-Emperor Seamount Chain, *J. Geophys. Res.*, *83*, 5989–6004.

White, R., and D. McKenzie (1989), Magmatism at rift zones: The generation of volcanic continental margins and flood basalts, *J. Geophys. Res.*, *94*, 7685–7729.

Yuen, D. A., R. Sabadini, and E. Boschi (1983), The dynamical equations of polar wander and the global characteristics of the lithosphere as extracted from rotational data, *Phys. Earth Planet. Inter.*, *33*, 226–242, doi:10.1016/0031-9201 (83)90124-3.

V. R. Barletta and R. Sabadini, Dipartimento di Scienze della Terra, Sezione Geofisica, Università degli Studi di Milano, Via L. Cicognara 7, I-20129 Milano, Italy. (valentina.barletta@unimi.it; roberto.sabadini@unimi.it)